WIRELESS COMMUNICATIONS AND MOBILE COMPUTING
Wirel. Commun. Mob. Comput. 2002; **2**:763–784 (DOI: 10.1002/wcm.76)

A blind coherent spatiotemporal processor of orthogonal Walsh-modulated CDMA signals

Sofiène Affes*,† and Paul Mermelstein
INRS-Télécommunications,
Université du Québec
800 de la Gauchetière Ouest, Suite 6900
Montréal, Québec, H5A1K6 Canada

Summary

A more efficient detection of orthogonal Walsh-modulated Code Division Multiple Access (CDMA) signals is required not only for better exploitation of current IS-95 CDMA systems but also for future cdma2000 3G networks. Integration of adaptive antennas at the base station has been recognized as one key lever to increasing capacity and spectrum efficiency. Prospective array-receiver solutions such as the 2-D-RAKE improve performance; however, in the absence of a pilot signal, they have to implement noncoherent detection. In this work, we propose a space-time processor that achieves coherent detection of orthogonal Walsh-modulated CDMA signals without a pilot. We assess its performance in spatially correlated Rayleigh-fading. Simulation results for voice links of 9.6 Kbps indicate that up to an antenna-correlation factor of 0.8, the proposed receiver outperforms the conventional 2-D-RAKE's capacity by 90% in nonselective fading. This gain shrinks fast at higher correlation factors. In selective fading, however, it maintains about a 130% gain in capacity over the entire correlation range. For data links of 153.6 Kbps, this performance advantage increases up to 180–200%. With high-speed mobiles, however, it vanishes quickly at correlation factors beyond 0.5. Overall, the capacity gains of the proposed spatiotemporal receiver structure increase with reduced relative Doppler (Doppler-frequency/symbol-rate ratio). This may arise from increased spatiotemporal diversity, higher transmission rates, and/or slower mobility.

*Correspondence to: Sofiène Affes, INRS-Télécommunications, Université du Québec, 800 de la Gauchetière Ouest, Suite 6900, Montréal, Québec, H5A1K6 Canada.
†E-mail: affes@inrs-telecom.uquebec.ca
Contract/grant sponsor: Bell/Nortel/NSERC Industrial Research Chair in Personal Communications.
Contract/grant sponsor: NSERC Research Grants Program.

KEY WORDS
space-time processing
smart/adaptive antennas
orthogonal Walsh modulation
IS-95 CDMA
cdma2000
diversity
spatial correlation
capacity

1. Introduction

A more efficient exploitation of current IS-95 CDMA systems (i.e. cdma-One) [1] and future cdma2000 3G networks (radio configurations 1 and 2) [2] requires enhanced detection of Walsh-modulated CDMA signals. Postponement of the exploitation of wideband carriers of 3.75 MHz until better market opportunities [3] puts even more pressure on maximizing the capacity of the Walsh-modulated CDMA systems currently deployed over narrowband carriers of 1.25 MHz.

Adaptive antenna arrays promise to satisfy this challenging demand for capacity arising from the large amount of wireless data to be supported in the future. In addition to providing spatial diversity, array receivers also achieve efficient interference reduction by spatial combining. To satisfy the current IS-95 standard [1], we are interested in blind array receivers in which no pilot signal is required.

Significant progress has been recently reported in developing blind array receivers for Walsh-modulated signals. For better exploitation of spatial diversity, noncoherent equal-gain combining (EGC) was proposed instead of sectorization [4,5]. For better exploitation of the antenna-processing capabilities of an array receiver, noncoherent EGC over antennas was replaced by noncoherent maximum ratio combining (MRC) [6] in a structure known as the two-dimensional RAKE (2-D-RAKE). Following these last steps in performance improvement of antenna-array receivers for Walsh-modulated signals, additional enhancements remain to be exploited until noncoherent EGC is completely replaced by coherent MRC in both space and time, without a pilot.

Implementation of coherent MRC combining requires timely estimates of the propagation vectors without phase ambiguities. Two structures that implement blind coherent MRC combining of Walsh-modulated signals have been recently studied [7]. They are based on noncoherent and iterative decision-directed training. We follow here a different path [8–11] and propose an adaptive channel identification procedure that exploits hard-decision symbol-estimation feedback. By successive simple upgrades of the feedback signal, we arrive at gradually improved array-receiver implementations ranging from the conventional 2-D-RAKE to a coherent spatiotemporal MRC combiner. The best receiver version has a one-dimensional space-time (1-D-ST) structure that jointly processes diversity fingers carrying out identification and combining in space and time.

The organization of the paper is as follows: In Section 2, we provide the data model and give a review of the EGC [4,5] and 2-D-RAKE combiners [6]. In Section 3, we propose incremental upgrades of the 2-D-RAKE that ultimately lead to a very efficient blind coherent spatiotemporal MRC combiner of Walsh-modulated signals. Section 4 assesses the performance of these receivers in spatially correlated Rayleigh-fading. Finally, we report our conclusions in Section 5. Results indicate that the proposed array receiver outperforms the conventional 2-D-RAKE resulting in significant capacity gains.

2. Formulation and Background

2.1. Assumptions and Model

We consider a CDMA cellular system in which each base station is equipped with M-receiving antennas. We are particularly interested in the uplink, but the proposed technique is also applicable to the downlink with similar advantages. We consider a multipath

environment with P paths. We assume that the multipath time-delays are perfectly estimated and tracked. Time acquisition and tracking are addressed in References [8] and [11] in which an efficient transceiver scheme combining synchronization and reception is proposed.

In the present IS-95 2G-standard [1] as well as in the future cdma2000 3G-standard (radio configurations 1 and 2) [2], information bits are coded by a convolutional encoder, grouped into $\log_2(L)$ bits, then coded into Walsh symbols, say $w_n \in \{1, \ldots, L\}$. For each symbol, the corresponding orthogonal Walsh sequence of length L is further spread by a spreading sequence up to the chip rate before final transmission. For the sake of simplicity, we do not identify separately the in-phase and quadrature components, but consider transmission over a complex channel.

At reception, the signal vector received at the M antennas is fed to a preprocessor, then to a set of L Walsh correlators, as shown in Figure 1. The preprocessor carries out baseband demodulation, matched chip-pulse filtering, sampling at the chip rate, A/D conversion, and despreading at the symbol rate. Each correlator outputs signal samples on P fingers that correspond to the P multipath components in a RAKE-like structure. Notice, however, that each finger is an $(M \times 1)$-dimensional vector denoted by $Z^i_{p,n}$, referred to as the post-correlation or despread vector of the i-th Walsh correlator for the p-th path at symbol iteration number n.

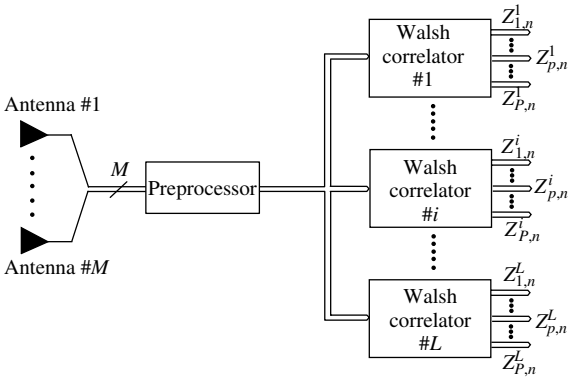

Fig. 1. Correlator structure at the base station for a desired user. The preprocessor implements baseband IQ demodulation, A/D conversion as well as sampling and despreading of the data at the appropriate rate. The M-dimensional vector $Z^i_{p,n}$ is the despread vector of the i-th Walsh correlator for the p-th path at the symbol iteration number n.

We assume that time-variations in the propagation characteristics are slow compared to the symbol duration and can be ignored over such an interval (i.e. Walsh sequence). Therefore, we can write the post-correlation vector $Z^i_{p,n}$ as follows:

$$\begin{aligned} Z^i_{p,n} &= G_{p,n}\psi_n\varepsilon_{p,n}\delta_{i,w_n} + N^i_{p,n} \\ &= G_{p,n}s^i_{p,n} + N^i_{p,n} \end{aligned} \tag{1}$$

where ψ_n^2 is the total received power and $\varepsilon^2_{p,n}$ for $p = 1, \ldots, P$ are the normalized power fractions over the P multipaths (i.e. $\sum_{p=1}^{P} \varepsilon^2_{p,n} = 1$). $G_{p,n}$ is the $(M \times 1)$-dimensional propagation vector over the p-th path, whose norm is fixed for convenience to $\sqrt{M}$ [9]. For each multipath-delay, we assume that the corresponding M diversity paths received at the different antennas are spatially correlated, in contrast to Reference [9] in which the paths were assumed uncorrelated. We retain the assumption that the additive noise vector $N^i_{p,n}$ is a spatially and temporally uncorrelated zero-mean complex Gaussian noise independent for each path and for each antenna. This assumption still holds when a large number of users are active even in the presence of spatial correlation when the complex correlation factor between each part of the antennas has a different phase from one mobile to another. Therefore, we aim to implement coherent MRC in both space and time, the optimal combiner in this case. Otherwise, for colored noise situations, we may incorporate the optimum or the multiuser combining solutions proposed in References [12] and [13], respectively; but that is beyond the scope of this paper. Because of the orthogonality of the Walsh symbols, the additive noise vector $N^i_{p,n}$ is independent and identically distributed over the L decision branches with a covariance matrix $R_N = \sigma_N^2 I_M$. Finally, the Kronecker symbol δ_{i,w_n} is the binary result at iteration n of correlating the received Walsh symbol w_n by the i-th Walsh correlator, and $s^i_{p,n} = \psi_n\varepsilon_{p,n}\delta_{i,w_n}$ is the corresponding multipath signal component over the p-th path, $p = 1, \ldots, P$.

On the basis of the data model above, we next introduce two representative space-time array-processing solutions for orthogonal Walsh-modulated CDMA signals (see Figure 2) that have been well covered in the literature. Later, we propose significant array-processing enhancements that lead through various incremental upgrades to a very efficient blind coherent spatiotemporal MRC combiner of Walsh-modulated CDMA signals (see Table I).

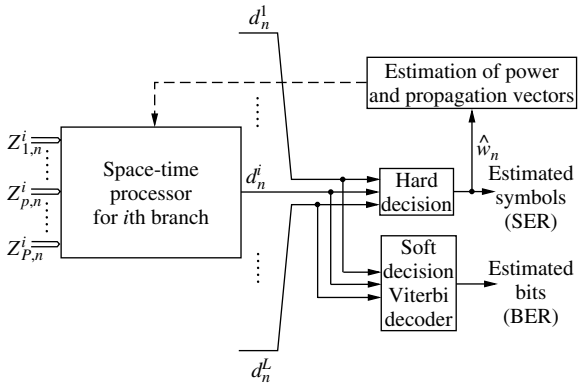

Fig. 2. Receiver structure at the base station for a desired user showing the spatiotemporal processor for the i-th Walsh-correlator branch of Figure 1.

2.2. Noncoherent Spatiotemporal Equal-gain Combining (EGC)

The first space-time array processor that replaces sectorization by an effective combining of multiple antenna-inputs is the noncoherent joint spatiotemporal equal-gain combiner [4,5], referred to here as Rx1 (see Table I). It simply sums at the output of each Walsh-correlator branch all the powers collected over the $M \times P$ diversity paths. For $i = 1, \ldots, L$, the decision variable at the output of the i-th Walsh-correlator branch is given by (see also summary in Table II):

$$d_n^i = \sum_{p=1}^{P} \|Z_{p,n}^i\|^2 / M \tag{2}$$

where the division by the number of antennas M is introduced for normalization. The L decision variables are then fed to a soft decision Viterbi decoder to retrieve the information bits (see Figure 2).

For power control, we need timely estimates of the received symbols (see Figure 2). Since the decision variables are decoded over relatively long symbol frames, we simultaneously estimate the received symbols by hard decision as follows (applies to all tested array receivers):

$$\hat{w}_n = \underset{i \in \{1, \ldots, L\}}{\text{argmax}} \left\{ d_n^i \right\} \tag{3}$$

This immediate decision allows estimation of the total received power $\hat{\psi}_n^2$ for power control by averaging $d_n^{\hat{w}_n} - \sum_{i \neq \hat{w}_n} d_n^i/(L-1)$ over a given number of symbols [4]. Here, we estimate the received power by smoothing as follows:

$$\hat{\psi}_{n+1}^2 = (1-\alpha)\hat{\psi}_n^2 + \alpha \max\left\{ d_n^{\hat{w}_n} - \hat{\sigma}_{\text{res}}^2, 0 \right\} \tag{4}$$

$$\hat{\sigma}_{\text{res}}^2 = (1-\alpha)\hat{\sigma}_{\text{res}}^2 + \alpha \frac{\sum_{i \neq \hat{w}_n} d_n^i}{L-1} \tag{5}$$

where $\alpha \ll 1$ is a smoothing factor and $\hat{\sigma}_{\text{res}}^2$ denotes the estimated variance of the residual interference in the decision variable of the estimated symbol $d_n^{\hat{w}_n}$.

The decision variable d_n^i sums the squares of $2MP$ real Gaussian variables with variance $\sigma^2 = \sigma_N^2/(2M)$ (i.e. the variance of the real/in-phase or imaginary/quadrature component of a complex element of $Z_{p,n}^i/\sqrt{M}$). For the correct-decision branch (i.e. $i = w_n$), the squares of the averages sum to ψ_n^2, and hence $d_n^{w_n}$ has a noncentral chi-square distribution with $2MP$ degrees of freedom and noncentrality parameter ψ_n^2 [14]. For a wrong-decision branch (i.e. $i \neq w_n$), all the Gaussian variables are zero-mean and hence d_n^i has a central chi-square distribution with $2MP$ degrees of freedom [14].

In Table III, we provide expressions for the probability density functions $f_D^c(d)$ and $f_D^e(d)$ of the decision variable d_n^i for the correct-decision branch (i.e. $i = w_n$) and for a wrong-decision branch (i.e. $i \neq w_n$), respectively. The mean $\overline{d} = \psi^2 \delta_{i,w_n} + P\sigma_N^2$ (i.e. $\sigma_{\text{res}}^2 = P\sigma_N^2$ in Equation (5)) and the variance $\sigma_d^2 = 2\psi^2\sigma_N^2\delta_{i,w_n}/M + P\sigma_N^4/M$ are given as well. $f_D^c(d)$ and $f_D^e(d)$ are illustrated in Figure 3(a) with the two curves in solid and dashed lines, respectively. The symbol error rate (SER) could be computed by numerical integration of the following probability

Table I. Description of the tested array receivers.

	Rx description	Notes	
		when $P = 1$	when $M = 1$
Rx1	Noncoherent joint spatiotemporal EGC combiner		
Rx2	Conventional 2-D-RAKE		Equiv. to Rx1
Rx3	Rx2 with coherent spatial MRC combining		
Rx4	Rx3 with common decision feedback	Equiv. to Rx3	
Rx5	Rx2 with coherent spatiotemporal MRC combining		
Rx6	Coherent joint spatiotemporal MRC combiner	Equiv. to Rx5	

Table II. The decision rule, the corresponding feedback signal, and the resulting phase ambiguities of the channel estimates for each of the tested array receivers (Rx1 does not implement channel identification).

	Decision rule	Feedback signal	Ambiguity
Rx1	$d_n^i = \dfrac{\sum_{p=1}^{P} \|Z_{p,n}^i\|^2}{M} = \dfrac{\|Z_n^i\|^2}{M}$	None	No id.
Rx2	$\hat{s}_{p,n}^i = \dfrac{\hat{G}_{p,n}^H Z_{p,n}^i}{M} \longrightarrow d_n^i = \sum_{p=1}^{P} \|\hat{s}_{p,n}^i\|^2$	$\widehat{s_{p,n}^{w_n}} = \hat{s}_{p,n}^{\hat{w}_n}$	$\phi_{p,n} \in [0, 2\pi]$
Rx3	$\hat{s}_{p,n}^i = \mathrm{Re}\left\{\dfrac{\hat{G}_{p,n}^H Z_{p,n}^i}{M}\right\} \longrightarrow d_n^i = \sum_{p=1}^{P} \|\hat{s}_{p,n}^i\|^2$	$\widehat{s_{p,n}^{w_n}} = \hat{s}_{p,n}^{\hat{w}_n}$	$\phi_{p,n} \in \{0, \pi\}$
Rx4	$\hat{s}_{p,n}^i = \mathrm{Re}\left\{\dfrac{\hat{G}_{p,n}^H Z_{p,n}^i}{M}\right\} \longrightarrow \hat{s}_n^i = \sum_{p=1}^{P} \hat{\varepsilon}_{p,n} \hat{s}_{p,n}^i \longrightarrow d_n^i = \|\hat{s}_n^i\|^2$	$\widehat{s_{p,n}^{w_n}} = \hat{\varepsilon}_{p,n} \hat{\psi}_n \ \ \mathrm{Sign}\left\{\hat{s}_n^{\hat{w}_n}\right\}$	All $\phi_{p,n} = \begin{cases} 0 \\ \pi \end{cases}$
Rx5	$\hat{s}_{p,n}^i = \mathrm{Re}\left\{\dfrac{\hat{G}_{p,n}^H Z_{p,n}^i}{M}\right\} \longrightarrow d_n^i = \hat{s}_n^i = \sum_{p=1}^{P} \hat{\varepsilon}_{p,n} \hat{s}_{p,n}^i$	$\widehat{s_{p,n}^{w_n}} = \hat{\varepsilon}_{p,n} \hat{\psi}_n$	All $\phi_{p,n} = 0$
Rx6	$d_n^i = \hat{s}_n^i = \mathrm{Re}\left\{\dfrac{\hat{H}_n^H Z_n^i}{M}\right\}$	$\widehat{s_n^{w_n}} = \hat{\psi}_n$	$\phi_n = 0$

expression (applies also to Rx2, Rx3, and Rx4):

$$\mathrm{Prob}\left(\{\hat{w}_n \neq w_n\}\right) = 1 - \left(\int_0^{+\infty} \int_0^{x} f_D^c(x) f_D^e(y)\, dx\, dy\right)^{L-1} \quad (6)$$

to allow a quantitative assessment and comparison of Rx1 with the other tested array receivers. However, the scope of this paper is not limited to an SER analysis. For simplicity, we resort here to a qualitative evaluation of the SER. Later we directly estimate the system-level performance in terms of capacity, the ultimate key figure used for performance assessment.

Intuitively, a larger overlap region under the two curves in Figure 3(a) indicates[‡] an increasing SER at the input of the soft decision Viterbi decoder and therefore a higher bit error rate (BER) at its output. It hence results in a capacity loss. In this regard, we shall see that Rx1 has the poorest performance among the tested array receivers (see Figure 3). In essence, this receiver exploits antenna diversity in addition to multipath diversity to attenuate the time-variations of the total received power (or equivalently the average fading) by noncoherent spatiotemporal EGC. Compared to sectorized single-antenna receivers, it improves the capacity by reducing power-control errors and the transmit power. However, Rx1 does not exploit the processing capabilities of antenna arrays to reduce the interference power.

2.3. 2-D-RAKE Combiner

To the best of our knowledge, the 2-D-RAKE was the first adaptive array-processing receiver structure proposed for Walsh-modulated CDMA signals [6]. This receiver, referred to as Rx2 (see Table I), is adaptive in that it carries out iterative channel identification in order to replace noncoherent spatial EGC by more efficient noncoherent spatial MRC. The blind channel identification step of Rx2 will be explained shortly below.

For now, assume that estimates of the propagation vectors with phase ambiguities are available at each iteration n (i.e. $\hat{G}_{p,n} \simeq \mathrm{e}^{-j\phi_{p,n}} G_{p,n}$). At the output of each Walsh-correlator branch for $i = 1, \ldots, L$, Rx2 first estimates the multipath signal component $\hat{s}_{p,n}^i$ over each path for $p = 1, \ldots, P$ by noncoherent spatial MRC:

$$\begin{aligned} \hat{s}_{p,n}^i &= \hat{G}_{p,n}^H Z_{p,n}^i / M \\ &\simeq \mathrm{e}^{j\phi_{p,n}} \psi_n \varepsilon_{p,n} \delta_{i,w_n} + \hat{G}_{p,n}^H N_{p,n}^i / M \\ &\simeq \mathrm{e}^{j\phi_{p,n}} s_{p,n}^i + \eta_{p,n}^i \end{aligned} \quad (7)$$

where the residual interference $\eta_{p,n}^i$ is zero-mean complex Gaussian with variance σ_N^2/M. Rx2 thereby implements the so-called 'antenna gain' by reducing

[‡] A larger overlap region suggests (1) larger integration values for the density functions and/or (2) larger integration domains over which these densities have nonnegligible numerical values. Both effects increase the integral value in Equation (6) and hence reduce the SER. Both theoretical and experimental SER curves in Reference [9] (we do not include them here for lack of space) confirm this explanation, which remains intuitive, however.

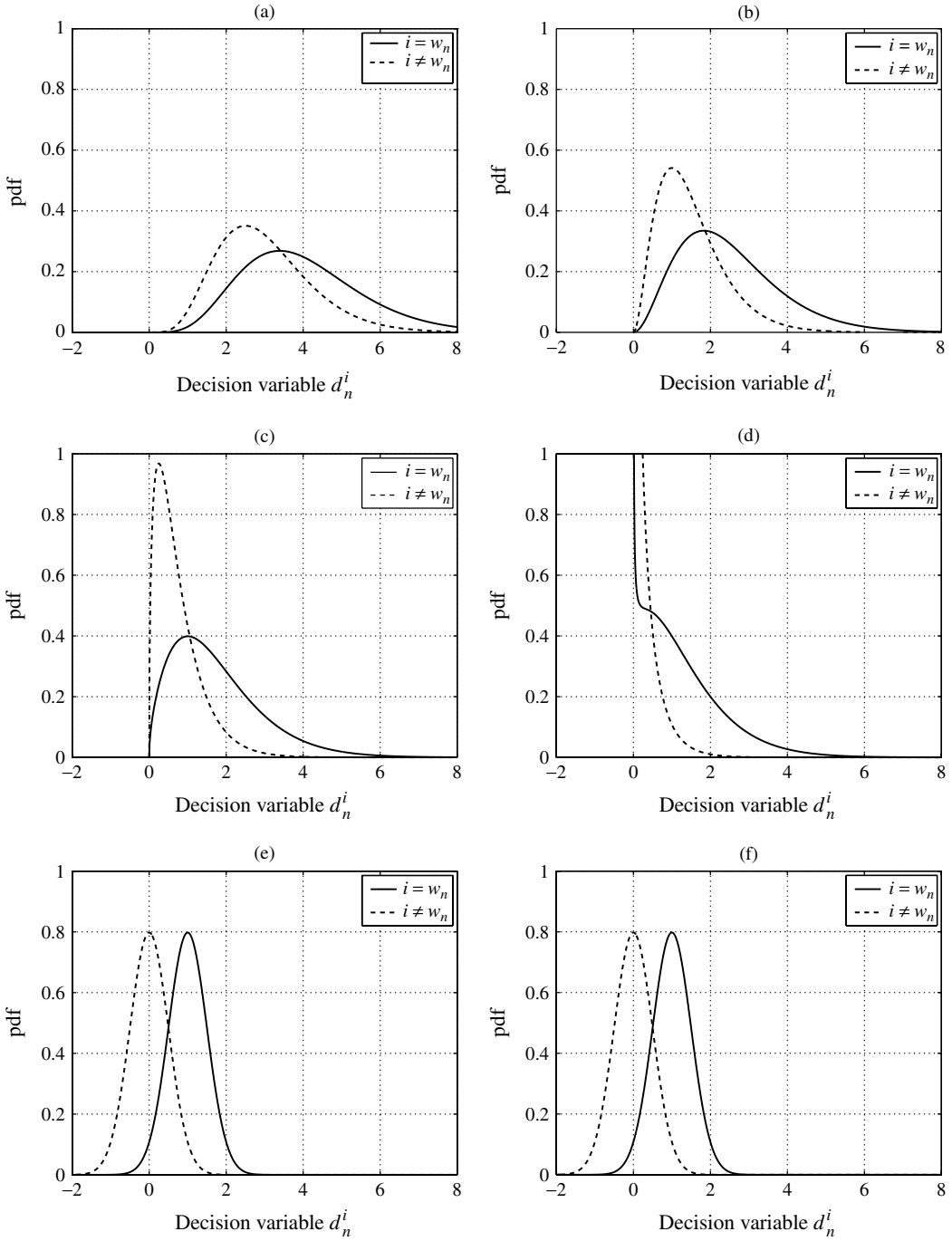

Fig. 3. Probability density function of the decision variable (correct decision in solid line, wrong decision in dashed line) for (a) Rx1; (b) Rx2; (c) Rx3; (d) Rx4; (e) Rx5; and (f) Rx6. Configuration: $M = 2$ antennas, $P = 3$ paths, perfect channel identification and power control (i.e. $\psi_n^2 = \psi^2 = 1$), and postcorrelation $SNR = 0$ dB (i.e. $\sigma_N^2 = 1$).

the level of interference by a factor M at the combiner output. Second, to alleviate the impact of the phase ambiguities $\phi_{p,n}$, Rx2 implements noncoherent temporal EGC of the multipath signal components by summing their powers. For $i = 1, \ldots, L$, the decision variable at the output of the i-th Walsh-correlator branch is given by (see also summary in Table II):

$$d_n^i = \sum_{p=1}^{P} \left| \hat{s}_{p,n}^i \right|^2 \tag{8}$$

Similarly to Rx1, these variables are fed to a soft Viterbi decoder (see Figure 2). They are also passed on to a hard-decision unit for symbol estimation using Equation (3). Power estimation follows using Equations (4) and (5).

The decision variable d_n^i sums the squares of $2P$ real Gaussian variables with variance $\sigma^2 = \sigma_N^2/(2M)$ (i.e. the variance of the real or imaginary part of the signal component $\hat{s}_{p,n}^i$ and also of the complex Gaussian residual noise $\eta_{p,n}^i$ with variance σ_N^2/M). For the correct-decision branch (i.e. $i = w_n$), the squares of the averages sum to ψ_n^2 and hence $d_n^{w_n}$ has a noncentral chi-square distribution with $2P$ degrees of freedom and noncentrality parameter ψ_n^2 [14]. For a wrong-decision branch (i.e. $i \neq w_n$), all the Gaussian variables are zero-mean and hence d_n^i has a central chi-square distribution with $2P$ degrees of freedom [14].

The probability density functions $f_D^c(d)$ and $f_D^e(d)$ are again provided in Table III along with the mean $\overline{d} = \psi^2\delta_{i,w_n} + P\sigma_N^2/M$ (i.e. $\sigma_{\text{res}}^2 = P\sigma_N^2/M$ in Equation (5)) and the variance $\sigma_d^2 = 2\psi^2\sigma_N^2\delta_{i,w_n}/M + P\sigma_N^4/M^2$. Notice the reduction of the noise power bias in the mean $\overline{d}$ as well as in the variance σ_d^2 as compared to Rx1 due to the decrease in the degrees of freedom k (i.e. EGC summations, see Table III). Later we seek further reduction of k to gradually improve the decision variable statistics (see Table III).

The density functions $f_D^c(d)$ and $f_D^e(d)$ are illustrated in Figure 3(b) in which the correct-decision curve is the solid line and the wrong-decision curve is the dashed line. As shown in Figure 3(b), noncoherent spatial MRC in the conventional 2-D-RAKE reduces the SER of Equation (6), intuitively indicated by the overlap region under the two curves. Because of a better reduction of interference, the noncoherent spatial MRC also improves the estimation of received power for power control. Both enhancements contribute to increasing capacity significantly.

As mentioned above, estimates of propagation vectors $\hat{G}_{p,n}$ are required to implement the noncoherent spatial MRC combining step in the 2-D-RAKE. Exploiting the fact that the interference vector in Equation (1) is an uncorrelated white noise vector, the propagation vector over each path $G_{p,n}$ can be identified as the principal eigenvector of the following matrix:

$$R_{Z_p} = E\left[Z_{p,n}^{w_n} Z_{p,n}^{w_n\,H}\right] = \psi^2\varepsilon_p^2 G_p G_p^H + \sigma_N^2 I_M$$
$$= \psi^2\varepsilon_p^2\left(\mathrm{e}^{-j\phi_p}G_p\right)\left(\mathrm{e}^{-j\phi_p}G_p\right)^H + \sigma_N^2 I_M \quad (9)$$

R_{Z_p} is the correlation matrix over each path of the despread vector $Z_{p,n}^{w_n}$ collected from the Walsh-correlator branch of the transmitted symbol w_n. In practice, each vector $G_{p,n}$ is estimated within an unknown phase ambiguity $\phi_{p,n}$ by an iterative principal component analysis (PCA) method based on a singular- or eigenvalue decomposition of the sample correlation matrix $\hat{R}_{Z_p}$ [6]. This sample matrix can be easily estimated after hard decision in Equation (3) by averaging or smoothing $Z_{p,n}^{\hat{w}_n} Z_{p,n}^{\hat{w}_n H}$. However, in the next section, we replace this iterative PCA method by an adaptive channel identification technique that is less complex and performs better.

In summary, the 2-D-RAKE [6] replaces the noncoherent spatial EGC of the early antenna-diversity combiners [4,5] by noncoherent spatial MRC. It achieves an antenna gain by reducing the interference power by a factor equal to the number of antennas and thereby improves capacity significantly. Following this first step in performance improvement of antenna-array receivers for Walsh-modulated signals, additional enhancements may be introduced until noncoherent EGC is completely replaced by coherent MRC in both space and time, without a pilot.

3. Blind Coherent Spatiotemporal Processor

In this section, we propose incremental upgrades of the 2-D-RAKE that ultimately lead to a very efficient blind coherent spatiotemporal MRC combiner of Walsh-modulated signals.

3.1. Adaptive Channel Identification

We propose an adaptive channel identification procedure that offers a unifying framework under a common structure called the spatiotemporal array receiver (STAR) [8–11] by equipping various combiners of Walsh-modulated signals with the same channel identification engine. By successive simple upgrades of its feedback signal, it implements gradually improved array receivers ranging from the conventional 2-D-RAKE to a blind coherent spatiotemporal MRC combiner.

This procedure, primarily developed for M-ary Phase Shift Keying (MPSK)-modulated signals and referred to as decision-feedback identification (DFI) [8,11], is adapted to the case of orthogonal

Walsh modulation as follows (applies to Rx2, Rx3, Rx4, and Rx5) [9,10]:

$$\hat{G}_{p,n+1} = \hat{G}_{p,n} + \mu_{p,n}\left(Z_{p,n}^{\hat{w}_n} - \hat{G}_{p,n}\widehat{s_{p,n}^{w_n}}\right)\widehat{s_{p,n}^{w_n}}^{*} \tag{10}$$

where $\mu_{p,n}$ is an adaptation step-size, possibly normalized[§], and $\widehat{s_{p,n}^{w_n}}$ is a feedback signal providing a selected estimate of the signal component after hard decision in Equation (3) (i.e. after estimation of $\hat{w}_n$, see Figure 2). Table II shows how a different choice of feedback signal leads to different combiners, except for Rx1, which requires neither channel identification nor signal feedback.

Notice that feeding back the signal-component estimate $\hat{s}_{p,n}^{\hat{w}_n}$ of Equation (7) as $\widehat{s_{p,n}^{w_n}}$ in Equation (10) readily enables implementation of Rx2, the 2-D-RAKE combiner discussed previously. This DFI-empowered version of Rx2 is used in the simulations section. In fact, the DFI procedure of Equation (10) offers an adaptive PCA implementation that is much more efficient than the iterative PCA method considered in the original 2-D-RAKE [6]. Its complexity order per symbol is only linear in the number of antennas M. It tracks time-varying channels faster because of its LMS-type nature ($\widehat{s_{p,n}^{w_n}}$ acts as a reference signal). With any random initialization $\hat{G}_{p,0}$ different from the null vector (here with norm $\sqrt{M}$), it converges to the propagation vector $G_{p,n}$ as the principal eigenvector of R_{Z_p} within a phase ambiguity $\phi_{p,n}$ (i.e. $\hat{G}_{p,n} \simeq \mathrm{e}^{-j\phi_{p,n}}G_{p,n}$). The iterative PCA method in Reference [6] is not decision-directed and results in a phase ambiguity that is almost random from one block iteration to another. With the DFI procedure, the phase ambiguity approaches a constant after convergence due to the very small gradient-perturbations in Equation (10) that update channel estimates from one iteration to the next. Below, we exploit this phase rotation $\phi_{p,n}$ as a degree of freedom to force its convergence to 0 or π by real-valued signal feedback (which restricts phase ambiguity drifts to negligible variations in the vicinity of ± 1). This gives rise to array-receiver structures that outperform Rx2 by coherent MRC combining, first implemented only in space, then in both space and time. In the following subsections, we resume the discussion of these receivers as listed in Tables I and II.

[§] Preferably $\|\hat{G}_{p,n}\|$ is also forced to $\sqrt{M}$ after each DFI update for increased stability (we do so in this work), although normalization of $\hat{G}_{p,n}$ to $\sqrt{M}$ is asymptotically guaranteed after convergence.

3.2. Coherent Spatial MRC Combining

In a new array-receiver structure referred to as Rx3 (see Table I), we exploit the flexibility of the DFI procedure and force the phase ambiguities to simple sign ambiguities (i.e. $\hat{G}_{p,n} \simeq \pm G_{p,n}$) as explained shortly below. Let us define $a_{p,n} \in [0, 1]$ and $\phi_{p,n} \in [0, 2\pi]$, as the amplitude and the phase of the normalized complex scalar product of $\hat{G}_{p,n}$ with $G_{p,n}$ (i.e. $\hat{G}_{p,n}^H G_{p,n}/M = a_{p,n}\mathrm{e}^{j\phi_{p,n}}$), knowing *a priori* that $a_{p,n}\mathrm{e}^{j\phi_{p,n}}$ will converge to ± 1. Thereby we replace the noncoherent spatial MRC combining step of the 2-D-RAKE by coherent spatial MRC combining. At the output of each Walsh-correlator branch for $i = 1, \ldots, L$, Rx3 estimates the multipath signal component over each path for $p = 1, \ldots, P$ as follows:

$$\begin{aligned}\hat{s}_{p,n}^{i} &= \mathrm{Re}\left\{\hat{G}_{p,n}^H Z_{p,n}^{i}/M\right\} \\ &= \left(a_{p,n}\mathrm{Re}\left\{\mathrm{e}^{j\phi_{p,n}}\right\}\right)\psi_n \varepsilon_{p,n}\delta_{i,w_n} \\ &\quad + \mathrm{Re}\left\{\hat{G}_{p,n}^H N_{p,n}^{i}/M\right\} \\ &\simeq \pm s_{p,n}^{i} + \mathrm{Re}\left\{\eta_{p,n}^{i}\right\}\end{aligned} \tag{11}$$

To alleviate the impact of the sign ambiguities $e^{j\phi_{p,n}} = \pm 1$, Rx3 implements noncoherent temporal EGC of the multipath signal components (i.e. sums their powers). Similarly to Rx2, it applies Equation (8) to compute the decision variables d_n^i (see also summary in Table II). These variables are then fed to a soft Viterbi decoder (see Figure 2). They are also passed on to a hard-decision unit for symbol estimation using Equation (3). Power estimation follows using Equations (4) and (5).

Feeding back the above real-valued signal-component estimate $\hat{s}_{p,n}^{\hat{w}_n}$ after hard decision as the feedback signal $\widehat{s_{p,n}^{w_n}}$ in the DFI procedure of Equation (10) forces the convergence of the amplitude $a_{p,n}$ to 1 and rotates the phase ambiguity $\phi_{p,n}$ along the shortest path to 0 or π from its initial value $\phi_{p,0}$. This process is illustrated in Figure 4 in which the DFI procedure updates the propagation vector estimate until the contribution $\left|a_{p,n}\mathrm{Re}\left\{\mathrm{e}^{j\phi_{p,n}}\right\}\right|$ in $\left|\hat{s}_{p,n}^{\hat{w}_n}\right|$ (see Equation 11) to the decision variable $d_n^{\hat{w}_n}$ in Equation (8) is maximized on average. Therefore, we have $\hat{G}_{p,n} \simeq \pm G_{p,n}$, where the sign ambiguity is independent from one path to another after convergence.

As a result, coherent spatial MRC combining in Equation (11) extracts the multipath signal component without noticeable distortion. More importantly, it reduces the variance of the residual interference

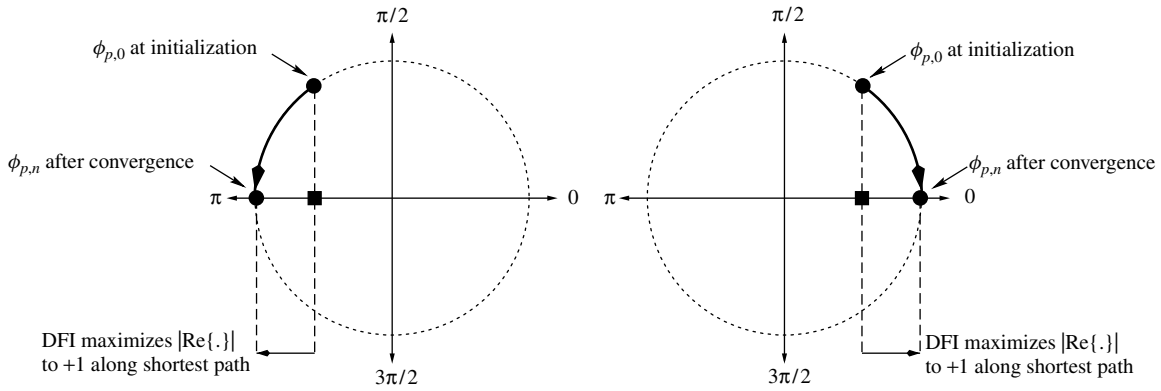

Fig. 4. Phase ambiguity rotation along shortest path to 0 or π on the unit circle ($\phi_{p,n}$ should read ϕ_n with Rx4).

Table III. Statistical characterization (pdf, average and variance) of the decision variable for each of the tested array receivers assuming perfect channel identification and power control (i.e. $\psi_n^2 = \psi^2$). $\mathcal{B}_q(x)$ and $\Gamma(x)$ are the q-th order modified Bessel function of the first kind and the Gamma function, respectively.

	Rx1	Rx2	Rx3	Rx4	Rx5	Rx6
Correct-decision branch ($i = w_n$)						
$f_D^c(d)$	Noncentral chi-square with k degrees of freedom and noncentrality parameter ψ^2 $\frac{1}{2\sigma^2}\left(\frac{d}{\psi^2}\right)^{\frac{k-2}{4}} \mathrm{e}^{-\frac{\psi^2+d}{2\sigma^2}} \mathcal{B}_{\frac{k}{2}-1}\left(\frac{\sqrt{d}\psi}{\sigma^2}\right)$				Gaussian $\frac{1}{\sqrt{2\pi}\sigma}\mathrm{e}^{-\frac{(d-\psi)^2}{2\sigma^2}}$	
$\overline{d}$	$k\sigma^2 + \psi^2$				ψ	
σ_d^2	$2k\sigma^4 + 4\sigma^2\psi^2$				σ^2	
Wrong-decision branch ($i \neq w_n$)						
$f_D^e(d)$	Central chi-square with k degrees of freedom $\frac{1}{\left(2\sigma^2\right)^{\frac{k}{2}}\Gamma\left(\frac{k}{2}\right)} d^{\frac{k}{2}-1}\mathrm{e}^{-\frac{d}{2\sigma^2}}$				Gaussian $\frac{1}{\sqrt{2\pi}\sigma}\mathrm{e}^{-\frac{d^2}{2\sigma^2}}$	
$\overline{d}$	$k\sigma^2$				0	
σ_d^2	$2k\sigma^4$				σ^2	
Parameters						
σ^2	$\frac{\sigma_N^2}{2M}$					
k	$2MP$	$2P$	P	1	—	

Re $\left\{\eta_{p,n}^i\right\}$ by half (i.e. $\sigma_N^2/(2M)$) relative to the original noncoherent spatial MRC step of the original 2-D-RAKE of Equation (7). The resulting 3 dB coherent detection gain is achieved without a pilot signal.

The decision variable d_n^i now sums the squares of P real Gaussian variables with variance $\sigma^2 = \sigma_N^2/(2M)$ (i.e. the variance of the real-valued multipath signal component $\hat{s}_{p,n}^i$ and also of the real Gaussian residual noise Re $\left\{\eta_{p,n}^i\right\}$). For the correct-decision branch (i.e. $i = w_n$), the squares of the averages sum to ψ_n^2 and hence $d_n^{w_n}$ has a noncentral chi-square distribution with P degrees of freedom

and noncentrality parameter ψ_n^2 [14]. For a wrong-decision branch (i.e. $i \neq w_n$), all the Gaussian variables are zero-mean and hence d_n^i has a central chi-square distribution with P degrees of freedom [14].

Table III gives the mean $\overline{d} = \psi^2\delta_{i,w_n} + P\sigma_N^2/(2M)$ (i.e. $\sigma_{\text{res}}^2 = P\sigma_N^2/(2M)$ in Equation (5) and the variance $\sigma_d^2 = 2\psi^2\sigma_N^2\delta_{i,w_n}/M + P\sigma_N^4/(2M^2)$ of the decision variables. Notice again the reduction of the noise power bias in the mean $\overline{d}$ as well as in the variance σ_d^2 as compared to Rx2 due to the decrease in the degrees of freedom k (i.e. EGC summations, see Table III).

The density functions $f_D^c(d)$ and $f_D^e(d)$ are illustrated in Figure 3(c). The SER of Equation (6) is further reduced by coherent spatial MRC in Rx3. Because of a better reduction of interference, it also improves the estimation of received power for power control. Both enhancements again contribute to increasing capacity significantly.

3.3. Common Decision Feedback

We further exploit the flexibility of the DFI procedure in an upgraded version of Rx3, referred to as Rx4 (see Table I), by introducing common decision feedback. It forces the phase ambiguities of the propagation vectors to a sign ambiguity identical over all multipaths as is explained shortly below. Hence, we replace the temporal EGC step of Equation (8) by temporal MRC. Assume that the estimates of the multipath power fractions $\hat{\varepsilon}_{p,n}^2 \simeq \varepsilon_{p,n}^2$ are available. At the output of each Walsh-correlator branch for $i = 1, \ldots, L$, Rx4 combines the multipath signal-component estimates of Equation (11) into a common signal-component estimate as follows:

$$\begin{aligned}\hat{s}_n^i &= \sum_{p=1}^{P} \hat{\varepsilon}_{p,n}\hat{s}_{p,n}^i \\ &= \left(\sum_{p=1}^{P} \hat{\varepsilon}_{p,n}\varepsilon_{p,n}a_{p,n}\text{Re}\left\{e^{j\phi_{p,n}}\right\}\right)\psi_n\delta_{i,w_n} \\ &\quad + \sum_{p=1}^{P} \hat{\varepsilon}_{p,n}\text{Re}\left\{\eta_{p,n}^i\right\} \\ &\simeq \pm s_n^i + \eta_n^i \end{aligned} \tag{12}$$

where $s_n^i = \psi_n\delta_{i,w_n}$ denotes the common signal component and η_n^i is the residual interference of the above temporal MRC combining step. Since the power fraction estimates are normalized to sum up to 1, the variance of η_n^i is $\sigma_N^2/(2M)$. To alleviate the effect of the sign ambiguity in the signal component estimate $\hat{s}_n^i$, we define the decision variables of Rx4 as follows for $i = 1, \ldots, L$ (see also summary in Table II):

$$d_n^i = \left|\hat{s}_n^i\right|^2 \tag{13}$$

Similarly to the previous receivers, these variables are fed to a soft Viterbi decoder (see Figure 2) and also passed on to a hard-decision unit for symbol estimation using Equation (3). On the other hand, the power fractions and the total received power are estimated for temporal combining and power control, respectively, as follows:

$$\hat{\varepsilon}_{p,n}^2 = \frac{\xi_{p,n}^2}{\hat{\psi}_n^2} \tag{14}$$

$$\hat{\psi}_n^2 = \sum_{p=1}^{P} \xi_{p,n}^2 \tag{15}$$

$$\begin{aligned}\xi_{p,n+1}^2 = (1-\alpha)\xi_{p,n}^2 + \alpha\max\left\{\left(\hat{s}_{p,n}^{\hat{w}_n}\right)^2\right. \\ \left. -\hat{\sigma}_{\text{res}}^2, 0\right\}\end{aligned} \tag{16}$$

$$\hat{\sigma}_{\text{res}}^2 = (1-\alpha)\hat{\sigma}_{\text{res}}^2 + \alpha\frac{\sum_{i\neq\hat{w}_n}\left|\hat{s}_n^i\right|^2}{L-1} \tag{17}$$

where $\alpha \ll 1$ is a smoothing factor and $\xi_{p,n}^2$ is an estimate of the received power from the p-th path (i.e. $\varepsilon_{p,n}^2\psi_n^2$).

In the DFI procedure of Equation (10), we now feed back $\hat{\varepsilon}_{p,n}\hat{\psi}_n\text{Sign}\left\{\hat{s}_n^{\hat{w}_n}\right\}$ as the reference signal $\widehat{s_{p,n}^{w_n}}$ for $p = 1, \ldots, P$. Notice that these reconstructed estimates of the multipath signal components are different from the soft-outputs $\hat{s}_{p,n}^{\hat{w}_n}$ of Equation (11) in that they carry the common sign of a hard decision over $\hat{s}_n^{\hat{w}_n}$. With this common decision feedback, we force the convergence of the amplitudes $a_{p,n}$ to 1 and the rotation of all the phase ambiguities $\phi_{p,n}$ to 0 or π. This occurs only when the contribution $\left|\sum_{p=1}^{P}\hat{\varepsilon}_{p,n}\varepsilon_{p,n}a_{p,n}\text{Re}\left\{e^{j\phi_{p,n}}\right\}\right|$ in $\left|\hat{s}_n^{\hat{w}_n}\right|$ (see Equation (12)) to the decision variable $d_n^{\hat{w}_n}$ of Equation (13) is maximized on average. Figure 4 no longer applies to the individual multipath phase ambiguities but now illustrates the convergence of the 'common' phase ambiguity, say ϕ_n, of the 'centroid' scalar product over all paths (i.e. $\sum_{p=1}^{P}\hat{\varepsilon}_{p,n}\varepsilon_{p,n}\hat{G}_{p,n}^H G_{p,n}/M = \sum_{p=1}^{P}\hat{\varepsilon}_{p,n}\varepsilon_{p,n}a_{p,n}e^{j\phi_{p,n}} = a_n e^{j\phi_n}$) along the shortest path from its initial value ϕ_0 to 0 or π. Notice that convergence of each multipath phase ambiguity $\phi_{p,n}$

to the common sign ambiguity does not necessarily follow the shortest path from its initial value. Compared to Rx3, slower convergence speed is therefore expected. However, we have $\hat{G}_{p,n} \simeq \pm G_{p,n}$ after convergence, where the sign ambiguity is identical over all paths.

The decision variable d_n^i now sums the square of a single real Gaussian variable with variance $\sigma^2 = \sigma_N^2/(2M)$ (i.e. the variance of the real-valued common signal component $\hat{s}_n^i$ or also of the real Gaussian residual noise η_n^i). For the correct decision branch (i.e. $i = w_n$), the square of the average is ψ_n^2 and hence $d_n^{w_n}$ has a noncentral chi-square distribution with 1 degree of freedom and noncentrality parameter ψ_n^2 [14]. For a wrong-decision branch (i.e. $i \neq w_n$), the Gaussian variable is zero-mean and hence d_n^i has a central chi-square distribution with 1 degree of freedom [14].

In Table III, we find the mean $\overline{d} = \psi^2 \delta_{i,w_n} + \sigma_N^2/(2M)$ (i.e. $\sigma_{\text{res}}^2 = \sigma_N^2/(2M)$ in Equation (17)) and the variance $\sigma_d^2 = 2\psi^2\sigma_N^2\delta_{i,w_n}/M + \sigma_N^4/(2M^2)$. Notice again the reduction of the noise power bias in the mean $\overline{d}$ as well as in the variance σ_d^2 as compared to Rx3 owing to the decrease in the degrees of freedom k (i.e. EGC summations, see Table III).

Figure 3(d) gives the associated density functions $f_D^c(d)$ and $f_D^e(d)$. Because of a better reduction of interference, common decision feedback also improves the estimation of received power for power control. Both enhancements again contribute to increasing capacity significantly.

3.4. Coherent 2-D-RAKE Spatiotemporal MRC Combining

We now upgrade Rx4 to a new version referred to as Rx5 (see Table I), in which we completely eliminate the common sign ambiguity in the propagation vector estimates. We explain below how this step is achieved without a pilot by positive-valued feedback in the DFI procedure. At the output of each Walsh-correlator branch for $i = 1, \ldots, L$, we still apply the temporal MRC combining step of Equation (12), only, the common signal component there no longer carries a sign ambiguity (i.e. $\hat{s}_n^i \simeq s_n^i + \eta_n^i$). Thus we replace the noncoherent decision variables of Rx4 in Equation (13) (i.e. a squarer) for $i = 1, \ldots, L$ by (see also summary in Table II):

$$d_n^i = \hat{s}_n^i \tag{18}$$

Similarly to Rx4, these variables are fed to a soft Viterbi decoder (see Figure 2) and also passed on to a hard-decision unit for symbol estimation using Equation (3). Estimation of the total received power and the power fractions follow using Equations (14) to (17).

In the DFI procedure of Equation (10), we now feed back $\hat{\varepsilon}_{p,n}\hat{\psi}_n$ as the reference signal $\widehat{s_{p,n}^{w_n}}$ for $p = 1, \ldots, P$. The *a priori* known Walsh-correlation output $\delta_{i,w_n} = +1$ for the correct branch (i.e. $i = w_n$) acts as a 'virtual pilot signal'. Hence we force $\widehat{s_{p,n}^{w_n}}$ to be real positive, that is, equate it to the received multipath amplitude estimate $\hat{\varepsilon}_{p,n}\hat{\psi}_n$. The symbol estimate $\hat{w}_n$ is now used only to select the despread vector $Z_{p,n}^{\hat{w}_n}$ in the DFI procedure and for power estimation. With this positive-valued common decision feedback, we force the convergence of the amplitudes $a_{p,n}$ to 1 and the rotation of the phase ambiguities $\phi_{p,n}$ to 0. This occurs only when the contribution $\sum_{p=1}^{P} \hat{\varepsilon}_{p,n}\varepsilon_{p,n}a_{p,n}\text{Re}\left\{e^{j\phi_{p,n}}\right\}$ in $\hat{s}_n^{\hat{w}_n}$ (see Equation (12)) to the decision variable $d_n^{\hat{w}_n}$ of Equation (18) is maximized on average. After convergence, we have $\hat{G}_{p,n} \simeq G_{p,n}$ for each multipath.

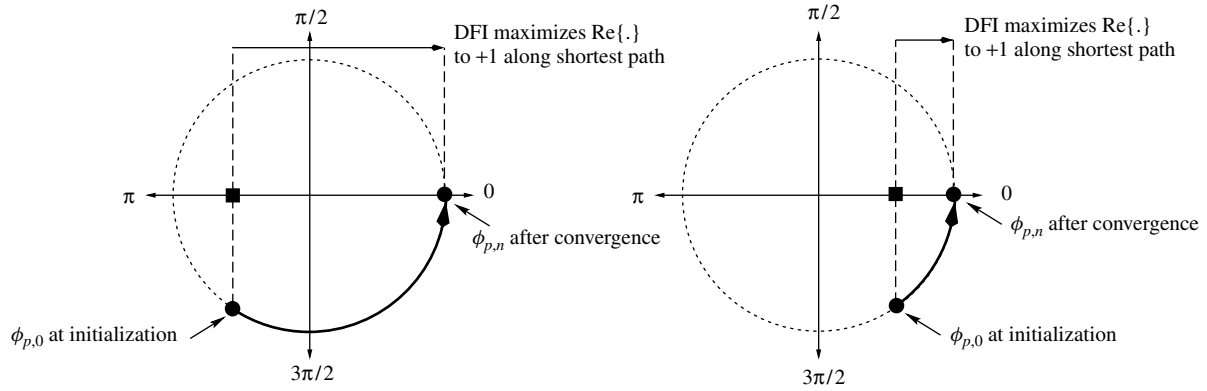

Fig. 5. Phase ambiguity rotation along shortest path to 0 on the unit circle ($\phi_{p,n}$ should read ϕ_n with Rx6).

Figure 5 illustrates the convergence of each multipath phase ambiguity $\phi_{p,n}$ to 0 along the shortest path from its initial value $\phi_{p,0}$. With Rx4, the phase ambiguity rotations would follow shorter paths to π if the initial 'common' phase ambiguity ϕ_0 is closer to π. With Rx3, the phase ambiguity rotations would follow even shorter separate paths to 0 or π. As we gradually upgrade the spatiotemporal processor STAR from Rx2 to Rx5, we impose more stringent constraints on the phase ambiguities and therefore introduce modes with slower convergence. To avoid the slower convergence with Rx5, we initially set STAR to Rx4 until convergence then switch it to Rx5. When ready to switch modes, we estimate the sign ambiguity of Rx4 from $\hat{s}_n^i$ of Equation (12) (after averaging over some iterations) and instantly eliminate it [15] from the propagation vector estimates of Rx4 for further DFI update with Rx5.

In summary, we can eliminate the noncoherent square summations and implement a coherent 2-D-RAKE spatiotemporal MRC combiner without a pilot. The decision variable d_n^i is real Gaussian with mean $\overline{d} = \psi_n \delta_{i,w_n}$ and variance $\sigma_d^2 = \sigma_N^2/(2M)$ (see Table III). The density functions $f_D^c(d)$ and $f_D^e(d)$ for the correct or wrong decisions are illustrated in Figure 3(e) with the two curves in solid and dashed lines, respectively. They suggest an additional reduction in the SER defined now as (applies also to Rx6):

$$\text{Prob}\left(\{\hat{w}_n \neq w_n\}\right) = 1 - \left(\int_{-\infty}^{+\infty}\int_{-\infty}^{x} f_D^c(x) f_D^e(y)\, dx\, dy\right)^{L-1} \quad (19)$$

However, the qualitative SER reduction is still indicated intuitively by the overlap region under the two curves of Figure 3(e). It translates into a significant capacity increase of Rx5 over Rx4.

3.5. Coherent Joint Spatiotemporal MRC Combining

So far, we exploited the flexibility of the DFI procedure in a 2-D-RAKE structure, that is, successive processing of diversity fingers in two dimensions: first in space over antennas, then in time over multipaths. Ultimately, we arrive at a coherent 2-D-RAKE spatiotemporal MRC combiner in Rx5. Yet further improvements are achievable by identifying and then combining all diversity fingers jointly in space and time with 1-D-ST structured versions of STAR. Of particular interest, the 1-D-ST counterpart of the 2-D-RAKE structured Rx5 receiver, referred to as Rx6 (see Table I), implements joint spatiotemporal MRC combining.

At the output of each Walsh-correlator branch for $i = 1, \ldots, L$, Rx6 first aligns the multipath despread vectors $Z_{p,n}^i$ for $p = 1, \ldots, P$ in an $MP \times 1$ spatiotemporal despread vector (see Equation (1)):

$$\underline{Z}_n^i = \begin{bmatrix} Z_{1,n}^i \\ \vdots \\ Z_{p,n}^i \\ \vdots \\ Z_{P,n}^i \end{bmatrix} = \begin{bmatrix} \varepsilon_{1,n} G_{1,n} \\ \vdots \\ \varepsilon_{p,n} G_{p,n} \\ \vdots \\ \varepsilon_{P,n} G_{P,n} \end{bmatrix} \psi_n \delta_{i,w_n} + \begin{bmatrix} N_{1,n}^i \\ \vdots \\ N_{p,n}^i \\ \vdots \\ N_{P,n}^i \end{bmatrix} = \underline{H}_n s_n^i + \underline{N}_n^i \quad (20)$$

where $\underline{H}_n^i$ is the $MP \times 1$ spatiotemporal propagation vector and $\underline{N}_n^i$ is the $MP \times 1$ spatiotemporal Gaussian noise vector with covariance matrix $R_{\underline{N}} = \sigma_N^2 I_{MP}$.

Second, exploiting the new data model of Equation (20), Rx6 merges the spatial and temporal MRC combining steps of Equations (11) and (12) in a joint spatiotemporal MRC combining step for $i = 1, \ldots, L$ as follows:[¶]

$$\begin{aligned} \hat{s}_n^i &= \sum_{p=1}^{P} \hat{\varepsilon}_{p,n} \text{Re}\left\{\hat{G}_{p,n}^H Z_{p,n}^i / M\right\} \\ &= \text{Re}\left\{\sum_{p=1}^{P} \hat{\varepsilon}_{p,n} \varepsilon_{p,n} \hat{G}_{p,n}^H G_{p,n} / M\right\} s_n^i \\ &\quad + \text{Re}\left\{\sum_{p=1}^{P} \hat{\varepsilon}_{p,n} \hat{G}_{p,n}^H N_{p,n} / M\right\} \\ &= \text{Re}\left\{\underline{\hat{H}}_n^H \underline{H}_n / M\right\} s_n^i + \text{Re}\left\{\underline{\hat{H}}_n^H \underline{N}_n / M\right\} \\ &= \text{Re}\left\{\underline{\hat{H}}_n^H \underline{Z}_n^i / M\right\} \\ &= \text{Re}\left\{a_n e^{j\phi_n}\right\} s_n^i + \eta_n^i \\ &\simeq s_n^i + \eta_n^i \end{aligned} \quad (21)$$

Given an estimate $\underline{\hat{H}}_n$ of the spatiotemporal vector $\underline{H}_n$, Rx6 in effect only implements $\text{Re}\left\{\underline{\hat{H}}_n^H \underline{Z}_n^i / M\right\}$ (see Table II). Similarly to Rx5, the resulting signal-component estimates $\hat{s}_n^i$ are assigned to the decision variables d_n^i using Equation 18) (see also summary in Table II). These variables are fed to a

[¶] Notice that the 'centroid' scalar product $\sum_{p=1}^{P} \hat{\varepsilon}_{p,n} \varepsilon_{p,n} \hat{G}_{p,n}^H G_{p,n} / M = a_n e^{j\phi_n}$ and the common phase ambiguity ϕ_n interpret now as the scalar product $\underline{\hat{H}}_n \underline{H}_n / M$ and the phase ambiguity of $\underline{\hat{H}}_n \simeq e^{j\phi_n} \underline{H}_n$ after convergence, respectively.

soft Viterbi decoder (see Figure 2) and also passed on to a hard-decision unit for symbol estimation using Equation (3). The total received power is estimated by

$$\hat{\psi}_{n+1}^2 = (1-\alpha)\hat{\psi}_n^2 + \alpha \max\left\{\left|\hat{s}_n^{\hat{w}_n}\right|^2 - \hat{\sigma}_{\text{res}}^2, 0\right\} \tag{22}$$

and the residual interference power $\hat{\sigma}_{\text{res}}^2$ by Equation (17).

With the same channel estimates, the new processing steps of Rx6 would suggest merely simple rearrangements of the data structure of Rx5. Rx5 and Rx6 would be identical and would have the same decision variables as supported by Table III and Figures 3(e) and 3(f) in the particular case of perfect power control and channel estimation. Actually, the benefits of joint spatiotemporal processing go beyond compact spatiotemporal data modeling when they reach the steps of signal combining and channel identification. Indeed, Rx6 replaces the P parallel DFI procedures of Equation (10) for all paths, referred to as 2-D-RAKE DFI, by a joint spatiotemporal DFI update:

$$\underline{\hat{\mathrm{H}}}_{n+1} = \underline{\hat{\mathrm{H}}}_n + \mu_n \left(\underline{\mathrm{Z}}_n^{\hat{w}_n} - \underline{\hat{\mathrm{H}}}_n \widehat{s_n^{w_n}}\right) \widehat{s_n^{w_n}}^* \tag{23}$$

where μ_n is an adaptation step-size, possibly normalized,[‖] and $\widehat{s_n^{w_n}} = \hat{\psi}_n$ is the spatiotemporal signal-component estimate. This 1-D-ST structured DFI procedure significantly reduces channel estimation and power-control errors and hence enables a valuable capacity gain over Rx5.

First, notice that estimation of the multipath power fractions of Equation (16) is no longer needed. It is implicitly embedded in the spatiotemporal channel estimate $\underline{\hat{\mathrm{H}}}_n$. Thereby we reduce the sensitivity of power smoothing to the residual interference floor $\hat{\sigma}_{\text{res}}^2$, higher for the weaker received power fractions $\xi_{p,n}^2$ in Equation (16) than for the total received power $\hat{\psi}_n^2$ in Equation (22). Furthermore, both accuracy and convergence speed[**] of the DFI procedure, which increase with higher feedback signal to noise power ratio [16]. The optimum adaptation step-size that minimizes estimation errors also varies with this ratio [16]. A joint DFI update with the total received power in the feedback signal $\widehat{s_n^{w_n}}$ in Equation (23) results in a better performance than separate DFI updates with fractioned powers over multipath feedback signals $\widehat{s_{p,n}^{w_n}}$ in Equation (10). It also requires the tuning of a single step-size μ_n instead of multiple step-sizes $\mu_{p,n}$. Joint DFI is hence faster in convergence and more robust to step-size selection than a 2-D-RAKE DFI. While the power variations of $\widehat{s_n^{w_n}}$ are 'equalized' by power control, those of $\widehat{s_{p,n}^{w_n}}$ are not. Increased stationarity of the feedback signal further increases the convergence speed and the performance advantage of joint DFI over 2-D-RAKE DFI in terms of both channel estimation and power-control errors.

Similarly to Rx5, we force the spatiotemporal feedback signal $\widehat{s_n^{w_n}}$ in the joint DFI procedure of Equation (23) to be real positive, that is, equate it to the total received amplitude estimate $\hat{\psi}_n$. We hence force the convergence of the amplitude a_n to 1 and the rotation of the phase ambiguity ϕ_n to 0. This occurs only when the contribution $\mathrm{Re}\left\{a_n e^{j\phi_n}\right\}$ in $\hat{s}_n^{\hat{w}_n}$ (see Equation (12)) to the decision variable $d_n^{\hat{w}_n}$ of Equation (18) is maximized on average, as illustrated in Figure 5. After convergence, we have $\underline{\hat{\mathrm{H}}}_n \simeq \underline{\mathrm{H}}_n$.

Notice that replacing the decision variable of Equation (18) by the squarer of Equation (13) gives rise to a 1-D-ST version of the 2-D-RAKE structured Rx4 (i.e. $\underline{\hat{\mathrm{H}}}_n \simeq \pm\underline{\mathrm{H}}_n$ after convergence). Similarly to Rx5, to speed up convergence, we start STAR with this faster version before we switch it to Rx6. Additionally, skipping the real part of the spatiotemporal MRC combiner of Equation (21) gives rise to a 1-D-ST structured version of STAR close to Rx2 in which the phase ambiguity $\phi_n \in [0, 2\pi]$ is common to all paths (i.e. $\underline{\hat{\mathrm{H}}}_n \simeq e^{i\phi_n}\underline{\mathrm{H}}_n$ after convergence). This version is not pursued further, it only illustrates the flexibility of the DFI procedure in providing various efficient versions of STAR, whether structured in a 1-D-ST or a 2-D-RAKE space-time processor of Walsh-modulated signals.

[‖] Preferably $\|\underline{\hat{\mathrm{H}}}_n\|$ is also forced to $\sqrt{M}$ after each DFI update for increased stability (we do so in this work), although normalization of $\underline{\hat{\mathrm{H}}}_n$ to $\sqrt{M}$ is asymptotically guaranteed after convergence (see footnote 2).

[**] Bear in mind that the data model is narrowband (see advantages of the postcorrelation model (PCM) in Reference [8] with respect to its narrowband nature.) and that the DFI procedure updates each element of the channel estimate as a single-tap filter, unlike wideband filters in which taps implement convoluted mixtures. Hence, neither misadjustment nor convergence speed (in both the average and mean square senses) change with the dimension of the narrowband observation [16].

In the case of a single path (i.e. $P = 1$ in nonselective fading), the 1-D-ST structured Rx6 becomes identical to the 2-D-RAKE structured Rx5 (see Table I). The 2-D-RAKE structured Rx3 and Rx4 become identical as well. In the case of a single receive antenna (i.e. $M = 1$ on the downlink for instance), Rx2 becomes identical to Rx1 (see Table I). On the other hand, differences between the 1-D-ST structured Rx6 and the 2-D-RAKE versions of STAR remain and gradually offer the same potential improvements over Rx1 and Rx2. In the general case, Rx6 version of STAR offers best performance. However, the intermediate upgrade versions Rx3, Rx4, and Rx5 turn out to be useful in spatially correlated nonselective fading (i.e. very poor diversity).

4. Performance Evaluation

4.1. Evaluation in Spatially Correlated Rayleigh-Fading

One major concern that arises when exploiting antenna arrays is the antenna spacing required at the base and/or the mobile-stations, in which space limitations may limit the benefits derived from use of multiple antennas. To minimize size and weight, antenna spacing should be kept to a minimum. As the antenna elements get closer, the spatial correlation between the paths to different antennas increases, thereby reducing the spatial diversity gain of the antenna array. Previous experimental studies [17–19] assessed the effect of correlation of Rayleigh-fading between two antennas on the performance of a simple diversity-combining scheme and revealed that spatial diversity cannot be exploited properly beyond a critical crosscorrelation threshold of 0.7. More recently, theoretical studies provided performance analyses for more advanced antenna-array combiners in spatially correlated fading, which arrived at a similar conclusion [20–23].

Here, we measure the performance of the tested array receivers (see Table I) in spatially correlated Rayleigh-fading by simulations at both link- and system-levels for Walsh-modulated CDMA signals. We evaluate the uplink performance in terms of the bit error rate, the required signal-to-noise ratio (SNR) at a BER of 10^{-3} and the resulting capacity, C, in number of users per cell. We assess how performance degrades as a function of the spatial correlation of Rayleigh-fading between the two receiving antennas (i.e. $M = 2$) at the base station.

We use the link- and system-level simulators described in Reference [4] with modifications that generate spatially correlated Rayleigh-fading. Multipath vector channel simulators such as Reference [24] take into account propagation conditions (i.e. angular spread, array geometry, locations, and so on ...) to model the spatial correlation between antennas. For each multipath, we simply use Jakes' model [25] to generate independent Rayleigh-fading paths to the two receive antennas. Then we force their correlation[††] to a real positive correlation factor, say ρ, identical over all multipaths. Thus, we have for $p = 1, \ldots, P$:

$$E\left[\psi_n^2 \varepsilon_{p,n}^2 G_{p,n} G_{p,n}^H\right] = \overline{\varepsilon}_p^2 \begin{bmatrix} 1 & \rho \\ \rho & 1 \end{bmatrix} \qquad (24)$$

where $\overline{\varepsilon}_p^2$ is the average power fraction. This simplifies the simulations by limiting the assessment of performance to sensitivity to a single spatial correlation parameter, the correlation factor ρ. We sample values of ρ between 0 and 1 to cover the entire range of the envelopes' crosscorrelation.

4.2. Simulation Setup

We simulate a narrowband CDMA system with 1.25 MHz bandwidth. This system is compatible with the IS-95 [1] and cdma2000-1x (for radio configurations 1 and 2) [2] standards. We also simulate a wideband CDMA system with 5 MHz bandwidth (i.e. 4×1.25 MHz). The cdma2000-3x wideband version of the cdma2000 standard [2] recommends a bandwidth of 3.75 MHz (i.e. 3×1.25 MHz). Nevertheless, the tested 5 MHz system will provide good indication on what to expect with cdma2000-3x by simple calibration. Both systems operate at a carrier frequency of 1.9 GHz. The narrowband system is nonselective with one path (i.e. $P = 1$). The wideband system is selective with three independent equal-power paths (i.e. $P = 3$ and $\overline{\varepsilon}_p^2 = 1/3$ for $p = 1, \ldots, 3$). For each path, a two-dimensional vector finger of independent Rayleigh-fading is generated with Jakes' model then spatially correlated using Equation (24) above.

Both systems serve mobiles with a voice-rate of 9.6 Kbps and a pedestrian speed of 1 Kmph. The Doppler

[††] We use the 'square-root' of the correlation matrix of Equation (24) as a spatial transform of the two independent Rayleigh-fading paths.

frequency is $f_D \simeq 2$ Hz. The voice-rate data is coded by a convolutional encoder at rate 1/3, sliced into segments of 6 coded bits then mapped into 64-ary Walsh symbols at a 4.8 Kbaud rate before interleaving with a 32×6 matrix (i.e. 40 ms frames of 192 symbols). Each Walsh symbol's sequence is further spread by factors 4 and 16 to match the chip rates of the narrow and wideband systems, respectively. Power control is updated every 1.25 ms (i.e. duration of 6 symbols) to instruct to the mobile to either increase or decrease its power by a constant step-size of 0.5 dB. This binary power-control transmission experiences 10% BER and a delay of 1.25 ms.

4.3. BER Results

In Figures 6 and 7, we provide performance results in terms of BER[‡‡] *versus* the input SNR per information bit for different values of ρ in the nonselective and selective fading environments, respectively. The curves indicate the following:

- For all methods, the degradation in performance becomes noticeable only at very high values of the correlation factor, whether the Rayleigh-fading is selective or not. This confirms that antenna arrays can still achieve efficient interference reduction despite a significant loss of spatial diversity[§§].
- The 2-D-RAKE structured array receivers that better exploit diversity are more sensitive to spatial correlation, more so in nonselective fading (see discussion in Section 4.6). An environment with poor diversity tends to minimize the gains owing to better combining of diversity fingers. Notice that the SNR loss from Figure 6(a) to 6(d) and from Figures 7(a) to 7(e) becomes more significant and abrupt at higher values of ρ. Only the SNR curves of the 1-D-ST structured Rx6 in Figure 7(f) remain

[‡‡] Convergence in both the average and mean square senses is relatively fast and requires less than two frames. All BER results are calculated at steady state convergence after excluding the first ten frames as a precaution.

[§§] We verified by simulations that a receiver with $M = 2$ antennas and $\rho = 1$ performs better than that with $M = 1$ antenna, although both situations offer the same spatial diversity.

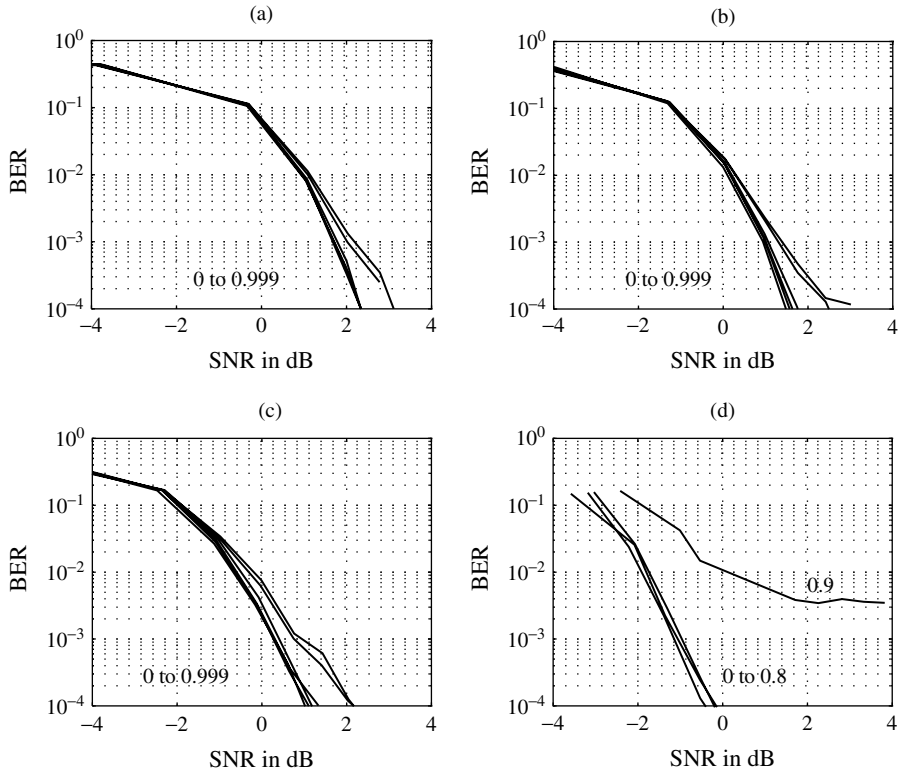

Fig. 6. BER *vs.* actual SNR per information bit in nonselective fading (i.e. $P = 1$) for different values of ρ (0, 0.7, 0.8, 0.9, 0.99, 0.999). (a) Rx1; (b) Rx2; (c) Rx3/Rx4 and (d) Rx5/Rx6.

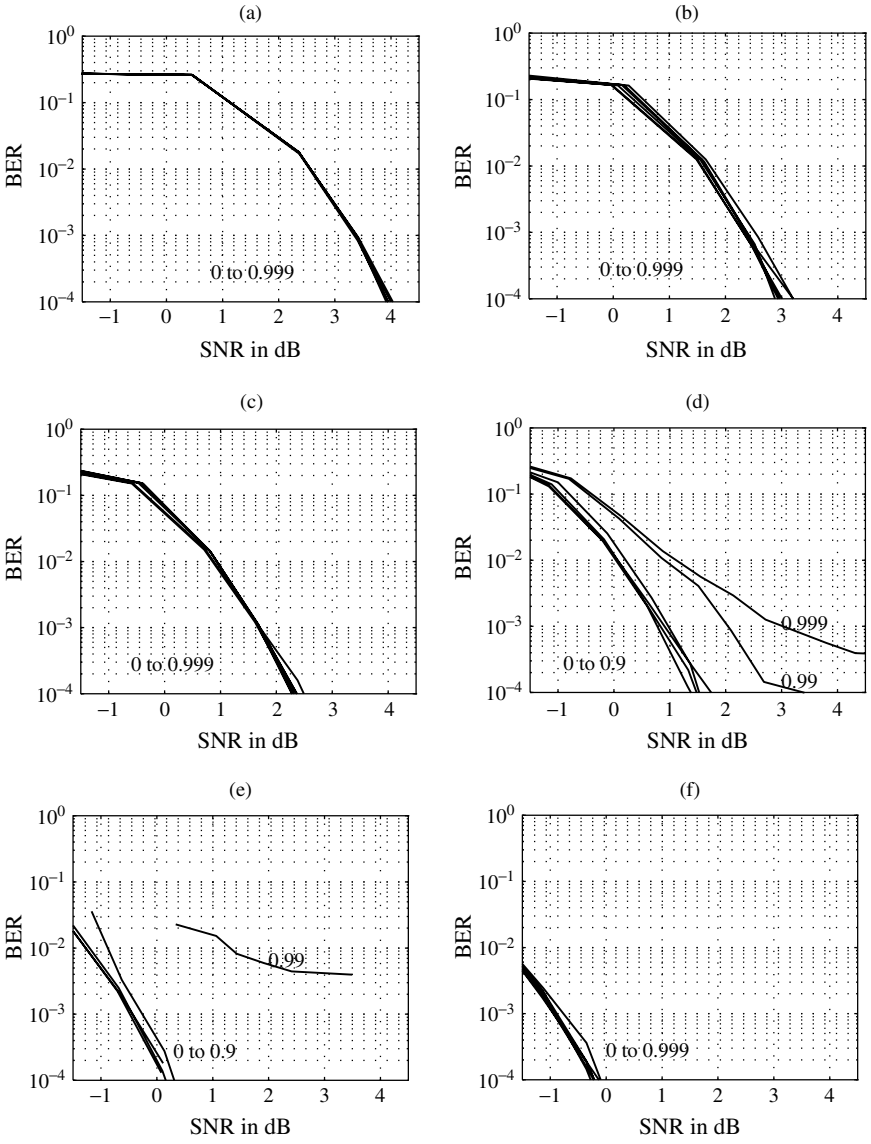

Fig. 7. BER *vs.* actual SNR per information bit in selective fading (i.e. $P = 3$) for different values of ρ (0, 0.7, 0.8, 0.9, 0.99, 0.999). (a) Rx1; (b) Rx2; (c) Rx3; (d) Rx4; (e) Rx5 and (f) Rx6.

almost constant. This confirms the advantages of the 1-D-ST DFI procedure in reducing channel estimation and power-control errors (see Subsection 3.5).

- In nonselective fading, the degradation in performance due to spatial correlation is more pronounced. Rx5/Rx6 should be used up to a correlation factor of about 0.8.[¶¶] For higher values of ρ, Rx3/Rx4 is preferred.
- In selective fading, multipath diversity reduces the sensitivity of the array receivers to spatial correlation (see discussion in Section 4.6). Among the 2-D-RAKE structured receivers, Rx5 should be used up to a correlation factor of about 0.9. For higher values of ρ, Rx4 is preferred up to a correlation factor of about 0.95, then Rx3 beyond 0.95. However, the 1-D-ST structured receiver Rx6 always outperforms the best of the 2-D-RAKE structured versions for any given value of ρ.

Overall, the proposed receiver upgrades always outperform Rx1 (i.e. noncoherent EGC

[¶¶] This value is close to the critical crosscorrelation threshold of 0.7 in References [17] and [18] beyond which spatial diversity cannot be exploited efficiently.

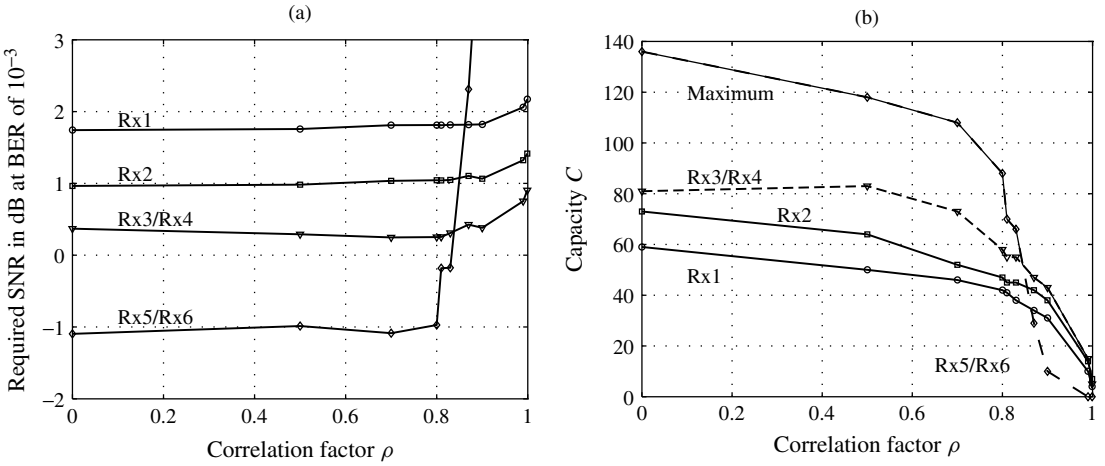

Fig. 8. Performance of the 1.25-MHz system at 9.6 Kbps *vs.* the correlation factor ρ for each of the tested array receivers with $M = 2$ antennas. (a) Required SNR and (b) Capacity C.

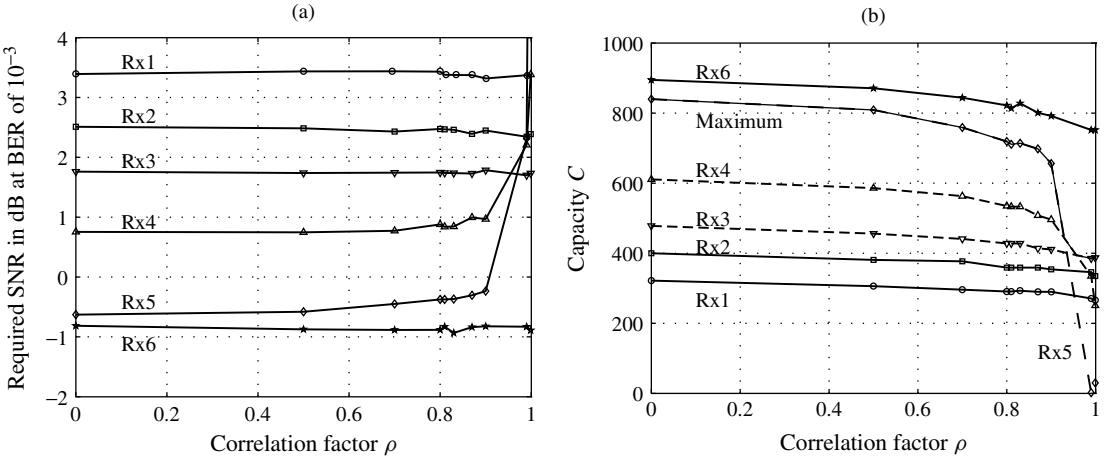

Fig. 9. Performance of the 5-MHz system at 9.6 Kbps *vs.* the correlation factor ρ for each of the tested array receivers with $M = 2$ antennas. (a) Required SNR and (b) Capacity C.

combiner) [4,5] and Rx2 (i.e. conventional 2-D-RAKE) [6] and offer the best performance for the tested values of the correlation factor ρ. In the following, we translate these BER improvements into SNR requirements and capacity gains.

4.4. Required SNR and Capacity Results

In Figures 8(a) and 9(a), we show the required SNR performance results of the tested array receivers for different values of ρ in both nonselective and selective fading environments.[‖‖] In nonselective fading, Figure 8(a) indicates up to a correlation factor of about 0.8 constant SNR gains of about 2.8 and 2 dB of Rx5/Rx6 over Rx1 [4,5] and Rx2 [6], respectively. At higher correlation factors, Rx3/Rx4 outperforms Rx1 and Rx2 by about 1.4 and 0.6 dB, respectively. On the other hand, Rx5/Rx6 sees its SNR performance deteriorate below that of Rx1 and Rx2 thereby confirming previous observation that array-receiver versions that better exploit diversity are more sensitive to spatial correlation, more so in nonselective fading (see discussion in Section 4.6). Indeed, in selective fading, Figure 9(a) indicates for all values of ρ almost constant SNR gains of Rx6 over Rx1 [4,5] and Rx2 [6] of about 4.3 and 3.4 dB, respectively.

From the above SNR results, we may compute the corresponding capacity C in terms of number of users

[‖‖] In Figure 8(a), Rx5/Rx6 cannot achieve the target BER of 10^{-3} for the last two values of ρ. In Figure 9(a), Rx5 cannot achieve the target BER of 10^{-3} for the last value of ρ.

per cell with a probability of outage of 1% using the computation procedure in Reference [4]. We assume a speech activity factor equal to 1 with probability $p_{\text{saf}} = 0.45$ and 1/8 otherwise [4]. Figures 8(b) and 9(b) show that the proposed array-receiver enhancements offer a significant increase in capacity over previous solutions [4–6] for Walsh-modulated CDMA signals in both selective and nonselective fading environments. In nonselective fading, Rx5/Rx6 provides the best capacity up to a correlation factor of about 0.8 while Rx3/Rx4 performs better at higher values of ρ (see semidashed curves in Figure 8b). The better of these two receivers at any correlation factor achieves the maximum capacity over the entire correlation range (see solid-line curve in Figure 8b). Up to a correlation factor around 0.8, it offers capacity gains over Rx1 [4,5] and Rx2 [6] of about 130 and 90%, respectively. These gains shrink dramatically at higher values of ρ. For extreme values of ρ approaching full correlation, Rx3/Rx4 performs nearly as well or worse than Rx2. In selective fading (see semidashed curves in Figure 9b), Rx5, Rx4, then Rx3 alternatively provide the maximum capacity among the 2-D-RAKE structured receivers (see solid-line curve in Figure 9b). The correlation thresholds lie approximately at 0.9 and 0.95. However, the 1-D-ST structured Rx6 offers the highest capacity gains over Rx1 [4,5] and Rx2 [6], about 180 and 130%, respectively.

Notice that the capacity curves of Figures 8(b) and 9(b) partly reflect the trend of the required SNR curves of Figures 8(a) and 9(a), respectively. Other factors such as channel estimation and power-control errors also impact the capacity results through variations of the received and transmitted power statistics in the incell and outcell interference [4]. In Figures 10 and 11, we show the channel identification mean square error (MSE) and the standard deviation of the total received power in both nonselective and selective fading, respectively. The new curves better explain the more severe degradation of capacity compared to SNR at extreme values of the correlation factor ρ, especially in nonselective fading (see discussion in Section 4.6). They also confirm the advantages of the 1-D-ST DFI against its 2-D-RAKE version in reducing both channel estimation and power-control errors as discussed in Subsection 3.5 (i.e. sensitivity of power smoothing to the residual interference floor is higher for the weaker received power fractions than for the total received power).

4.5. High Data-Rate and High-Mobility Applications

To provide evaluation results for a high data-rate application, we simulate data links at 153.6 Kbps in the 5 MHz system***. We use the same wideband simulation environment and assume a data activity factor equal to 1 with probability $p_{\text{daf}} = 1$ (i.e. noninterrupted transmission). We also use the same parameters for coding, Walsh mapping, and symbol interleaving. Figure 12 shows almost constant SNR and capacity curves over the entire range of ρ, suggesting a relatively weaker sensitivity of all array receivers

*** For the sake of simplicity, we keep the maximum BER to 10^{-3}.

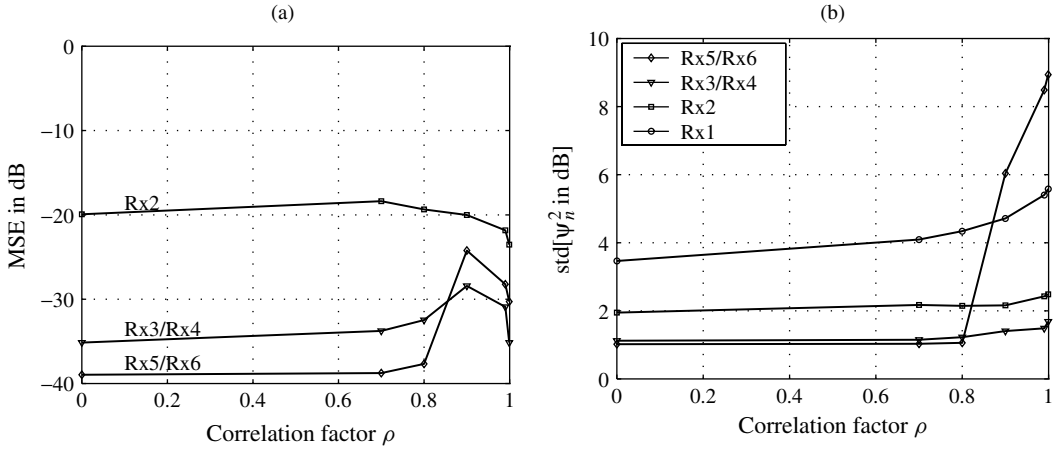

Fig. 10. Performance of the 1.25-MHz system at 9.6 Kbps *vs.* the correlation factor ρ for each of the tested array receivers with $M = 2$ antennas (postcorrelation $SNR = 0$ dB). (a) MSE of channel identification (for all array receivers but Rx1) and (b) Standard deviation of received power ψ_n^2.

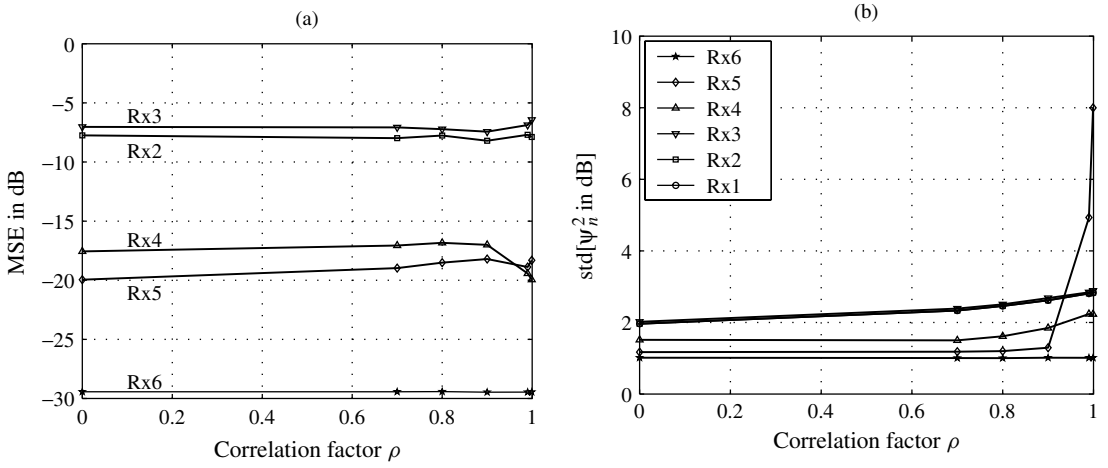

Fig. 11. Performance of the 5-MHz system at 9.6 Kbps *vs.* the correlation factor ρ for each of the tested array receivers with $M = 2$ antennas (postcorrelation $SNR = 0$ dB). (a) MSE of channel identification (for all array receivers but Rx1) and (b) Standard deviation of received power ψ_n^2.

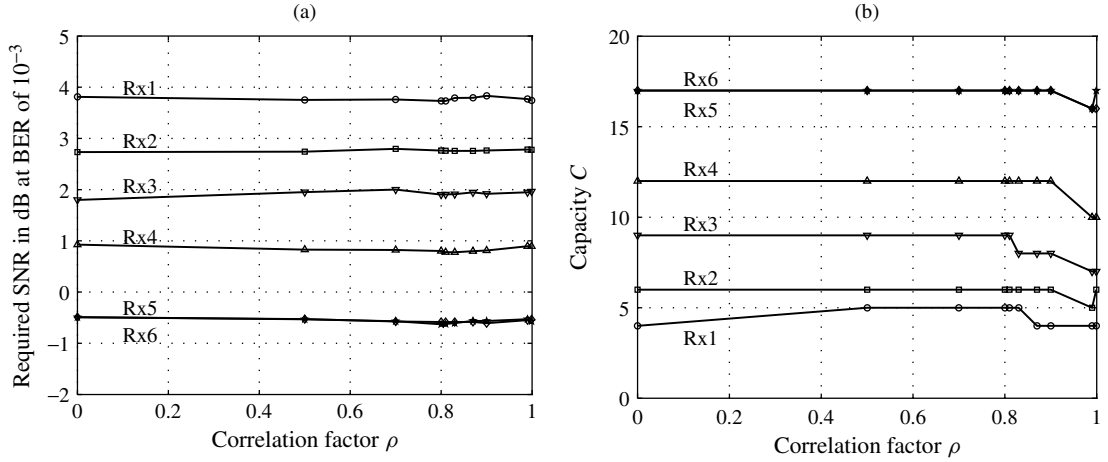

Fig. 12. Performance of the 5-MHz system at 153.6 Kbps with low speed (i.e. 1 Kmph) *vs.* the correlation factor ρ for each of the tested array receivers with $M = 2$ antennas. (a) Required SNR and (b) Capacity C.

to spatial correlation at higher data rates (see discussion in Section 4.6). While the SNR gain of Rx6 over previous solutions is almost in the same range as in Figure 9(a), its capacity advantage over Rx1 [4,5] and Rx2 [6] is more significant, in the range of 240 and 180%, respectively.

To assess the effect of the Doppler spread on performance, we increase the mobile speed of the data links from 1 to 50 Kmph (i.e. $f_D \simeq 90$ Hz). Figure 13(a) indicates that all receiver versions exact severe SNR losses,[†††] suggesting a relatively stronger sensitivity to spatial correlation at higher mobility (see discussion in Section 4.6). The structures that exploit spatiotemporal diversity better suffer most from mobility and see their SNR performance degrade most at a correlation factor higher than 0.9. The resulting shrinkage in SNR gaps across receiver versions leaves no margin for capacity gains. Figure 13(b) indicates that no receiver version except Rx6 can accommodate more than a single mobile at 153.6 Kbps. In contrast, the 1-D-ST structured Rx6 accommodates three mobiles thereby offering a 200% gain over all other receiver versions up to a correlation factor of 0.5. In the correlation-factor range of 0.5–0.9, capacity drops to 1 and above 0.9 to zero. The corresponding 0-capacity

[†††] In Figure 13(a), Rx6 cannot achieve the target BER of 10^{-3} for the last two values of ρ and Rx5 cannot achieve the target BER of 10^{-3} for the last value of ρ.

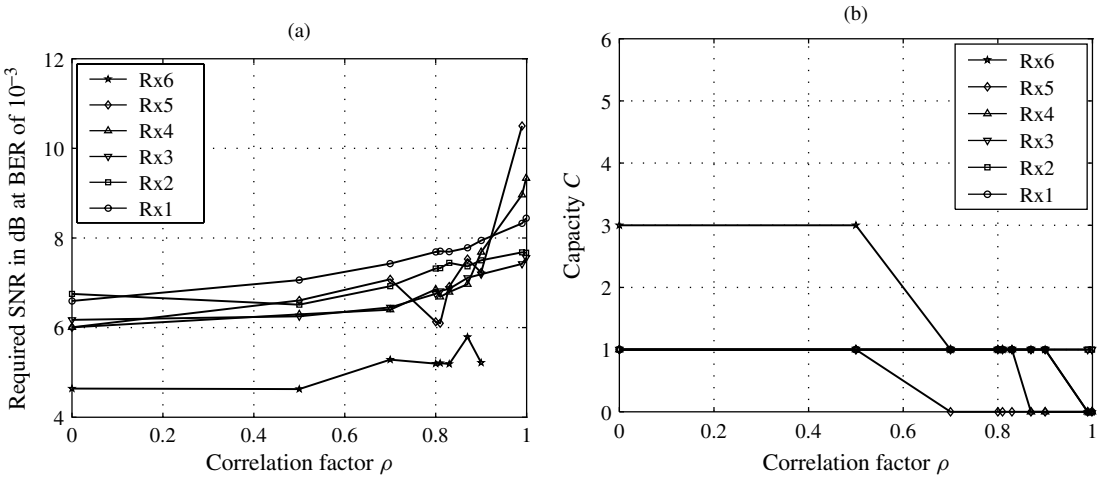

Fig. 13. Performance of the 5 MHz system at 153.6 Kbps with high speed (i.e. 50 Kmph) *vs.* the correlation factor ρ for each of the tested array receivers with $M = 2$ antennas. (a) Required SNR and (b) Capacity C.

thresholds for Rx4 and Rx5 are lower at 0.85 and 0.5, respectively.

4.6. Discussion

In the light of the simulations results above, we attribute degradation in performance of the most sophisticated spatiotemporal receivers to a common factor, that is, channel identification in worsening conditions due to faster channel-parameter variations and poorer diversity. Time-variations of the channel increase with the normalized Doppler $f_D T$, that is, at lower transmission rates and/or higher mobility. They also increase in poorer diversity situations[‡‡‡], that is, in nonselective fading, with spatially correlated antennas, and/or smaller antenna arrays[§§§].

The receivers that better exploit spatiotemporal diversity by more efficient use of spatiotemporal processing demand more precise channel identification. Rx3 forces the multipath phase ambiguities to 0 or π. Rx4 forces all the multipath phase ambiguities to a common 0 or π. Rx5 and Rx6 both force all the multipath phase ambiguities to a common 0. These more stringent requirements of the enhanced receivers impose extra demands on channel tracking, which become even more difficult to attain in worsening channel conditions (see discussion about increasing convergence time of more enhanced receivers in Section 3.4). Joint DFI, however, better exploits diversity advantages in channel identification and makes the 1-D-ST Rx6 more robust to faster channel-parameter variations as compared to the other proposed 2-D-RAKE structured Rx3, Rx4, and Rx5.

In the frequency-selective high-rate/low-mobility reference case of Figure 12, we can see the net benefits of the proposed spatiotemporal processing improvements at relatively very good channel conditions. The impact of spatial correlation there is almost negligible for correlation factors below 0.8–0.9. In the frequency-selective low-rate low-mobility situation of Figure 9, which increases the normalized Doppler $f_D T$ by a factor of 16, we start to notice significant performance degradation of the 2-D-RAKE structured Rx3, Rx4, and Rx5 due to spatial correlation, particularly at extreme values. The effect of spatial correlation is still negligible on the 1-D-ST structured Rx6 for correlation factors below 0.8. In the frequency-selective high-rate high-mobility situation of Figure 13, which increases the normalized Doppler $f_D T$ by a factor of 50 relative to the reference situation, effects of spatial correlation on performance are even more significant and now reach those of the 1-D-ST structured Rx6. Joint DFI makes Rx6 much more robust to worsening channel conditions. It postpones first signs of significant performance degradation of Rx6 to much more adverse channel conditions

[‡‡‡] We mean particular increase in the variations of the total received power, which are smoother when averaging fades over an increasing number of spatiotemporal diversity fingers.

[§§§] We did not investigate this dimension, although it suggests ways for exploiting the potential performance advantage of the proposed array receivers in more adverse channel conditions by increasing the number of receive antennas (see results with Binary Phase Shift Keying (BPSK)/Quadrature Phase Shift Keying (QPSK) modulations in Reference [9]).

as compared to 2-D-RAKE structured Rx3, Rx4, and Rx5. Compared to the frequency-selective low-rate low-mobility situation of Figure 9, the frequency-nonselective low-rate low-mobility case of Figure 8 indicates increased sensitivity to spatial correlation at lower correlation factors due to poorer time diversity. It confirms channel identification in worsening/improving conditions as the main factor that drives the losses/gains of the proposed array receivers with enhanced spatiotemporal processing over previous receiver structures for Walsh-modulated signals [4–6].

5. Conclusion

We proposed a space-time processor that achieves coherent detection of orthogonal Walsh-modulated CDMA signals without a pilot. We followed an upgrade path that transformed the conventional 2-D-RAKE into an efficient 1-D-ST structured coherent spatiotemporal MRC combiner. Joint identification and combining of diversity fingers over space and time in a 1-D-ST structure is found to outperform 2-D-RAKE receivers in which processing is separate in space and time. We assessed the performance of the new receiver in spatially correlated Rayleigh-fading. Simulation results for voice links of 9.6 Kbps indicate that up to a correlation factor of 0.8, the proposed receiver outperforms the conventional 2-D-RAKE's capacity by 90% in nonselective fading. This gain shrinks fast at higher correlation factors. In selective fading, however, the proposed 1-D-ST receiver maintains about 130% gain in capacity over the entire correlation range. For data links of 153.6 Kbps, this performance advantage increases up to 180–200%. With high-speed mobiles, however, it vanishes quickly at correlation factors beyond 0.5. Overall, the capacity gains of the one-dimensional spatiotemporal receiver structure increase with reduced relative Doppler (Doppler-frequency/symbol-rate ratio). This may arise from increased spatiotemporal diversity, higher transmission rates, and/or slower mobility.

Acknowledgements

This work was supported by the Bell/Nortel/NSERC Industrial Research Chair in Personal Communications and by the NSERC Research Grants Program.

References

1. *An Overview of the Application of Code Division Multiple Access (CDMA) to Digital Cellular Systems and Personal Cellular Networks*. Qualcomm: USA, 1992.
2. 3rd Generation Partnership Project 2, Physical Layer Standard for cdma2000 Spread Spectrum Systems, Release A, 3GPP2 C.S0002-A Version 5.0, July 2001.
3. Langer J, Larsson G. CDMA2000—A world view. *Ericsson Review* 2001; **3**: 150–158.
4. Jalali A, Mermelstein P. Effects of diversity, power control, and bandwidth on the capacity of microcellular CDMA systems. *IEEE Journal on Selected Areas in Communications* 1994; **12**(5): 952–961.
5. Jalloul LMA, Holtzman JM. Performance analysis of DS/CDMA with noncoherent M-ary orthogonal modulation in multipath fading channels. *IEEE Journal on Selected Areas in Communications* 1994; **12**(5): 862–870.
6. Naguib AF, Paulraj A. Performance of wireless CDMA with M-ary orthogonal modulation and cell site antenna arrays. *IEEE Journal on Selected Areas in Communications* 1996; **14**(9): 1770–1783.
7. Thompson JS, Grant PM, Mulgrew B. Algorithms for coherent diversity combining of M-ary orthogonal signals. *IEEE Journal on Selected Areas in Communications* 1999; **17**(11): 1886–1899.
8. Affes S, Mermelstein P. A new receiver structure for asynchronous CDMA: STAR—the spatio-temporal array-receiver. *IEEE Journal on Selected Areas in Communications* 1998; **16**(8): 1411–1422.
9. Affes S, Mermelstein P. Signal processing improvements for smart antenna signals in IS-95 CDMA. In *Proc. IEEE PIMRC '98*, Vol. II, Boston, USA, 8–11 September 1998; pp. 967–972.
10. Affes S, Mermelstein P. Performance of a CDMA beamforming array-receiver in spatially-correlated Rayleigh-fading multipath. In *Proc. IEEE VTC '99*, Vol. 1, Houston, USA, 16–20 May 1999; pp. 249–253.
11. Cheikhrouhou K, Affes S, Mermelstein P. Impact of synchronization on performance of enhanced array- receivers in wideband CDMA networks. *IEEE Journal on Selected Areas in Communications* 2001; **19**(12): 2462–2476.
12. Hansen H, Affes S, Mermelstein P. A beamformer for CDMA with enhanced near-far resistance. In *Proc. IEEE ICC '99*, Vol. 3, Vancouver, Canada, 6–10 June 1999; pp. 249–253.
13. Affes S, Hansen H, Mermelstein P. Interference subspace rejection: A framework for multiuser detection in wideband CDMA. *IEEE Journal on Selected Areas in Communications* 2002; **20**(2): 287–302.
14. Proakis JG. *Digital Communications*. 3rd edition, McGraw-Hill: New York, 1995.
15. Affes S, Louzi A, Kandil N, Mermelstein P. A high capacity CDMA array-receiver requiring reduced pilot power. *In Proc. of IEEE GLOBECOM 2000*, Vol. 2, San Francisco, USA, November 27–December 1 2000; pp. 910–916.
16. Affes S, Mermelstein P. Comparison of pilot-assisted and blind CDMA array-receivers adaptive to Rayleigh fading rates. *In Proc. IEEE PIMRC '99*, Vol. 3, Osaka, Japan, 12–15 September 1999; pp. 1186–1192.
17. Lee WC-Y. Effects on correlation between two mobile radio base-station antennas. *IEEE Transactions on Communications* 1973; **21**(11): 1214–1224.
18. Adachi F, Feeney MT, Williamson AG, Parsons JD. Crosscorrelation between the envelopes of 900 MHz signals received at a mobile radio base station site. *IEE Proceedings* 1986; **133**(6): 506–512.
19. Turkmani AMD, Arowojolu AA, Jefford PA, Kellett CJ. An experimental evaluation of the performance of two-branch

space and polarization diversity schemes at 1800 MHZ. *IEEE Transactions on Vehicular Technology* 1995; **44**(2): 318–326.
20. Salz J, Winters J. Effect of fading on adaptive arrays in digital mobile radio. *IEEE Transactions on Vehicular Technology* 1994; **43**(4): 1049–1057.
21. Cui J, Sheikh AUH, Falconer DD. BER analysis of optimum combining and maximal ratio combining with channel correlation for dual antenna systems. In *Proc. IEEE VTC '97*, Vol. 1, Phoenix, USA, 4–7 May 1997; pp. 150–154.
22. Simon MK, Alouini M-S. A unified performance analysis of digital communications with dual selective combining diversity over correlated Rayleigh and Nakagami-m fading channels. *IEEE Transactions on Communications* 1999; **47**(1): 33–43.
23. Pham TD, Balmain KG. Multipath performance of adaptive antennas with multiple interferers and correlated fadings. *IEEE Transactions on Vehicular Technology* 1999; **48**(2): 342–352.
24. Stéphenne A, Champagne B. Effective multi-path vector channel simulator for antenna array systems. *IEEE Transactions on Vehicular Technology* 2000; **49**(11): 2370–2381.
25. Jakes WC (ed.). *Microwave Mobile Communications*. IEEE Press: New York, 1994.

Authors' Biographies

Sofiène Affes received the Diplôme d'Ingénieur in electrical engineering in 1992, and the Ph.D. degree in signal and image processing in 1995, both from the École Nationale Supérieure des Télécommunications, Paris, France.

He has been since with INRS-Telecommunications, University of Quebec, Montreal, Canada, as a research associate from 1995 to 1997, then as an assistant professor up to 2000. Currently he is an associate professor in the Personal Communications Group. His research interests are in statistical signal and array processing, synchronization, and multiuser detection in wireless communications. Previously, he was involved in the European ESPRIT projects 2101 ARS on speech recognition in adverse environments in 1991, and 6166 FREETEL on hands-free telephony from 1993 to 1994. In 1997, he participated in the major program in personal and mobile communications of the Canadian Institute for Telecommunications Research. Since 1998, he has been leading the radio-design and signal processing activities of the Bell/Nortel/NSERC Industrial Research Chair in Personal Communications at INRS-Telecommunications.

Paul Mermelstein received the B.Eng. degree in engineering physics from McGill University, Montreal, Canada, in 1959, and the S.M., E.E., and D.Sc. degrees in electrical engineering from the Massachusetts Institute of Technology, Cambridge, MA, in 1960, 1963, and 1964, respectively.

From 1964 to 1973, he was a member of the technical staff in the Speech and Communications Research Department of Bell Laboratories, Murray Hill, NJ. From 1973 to 1977, he was a member of the research staff at Haskins Laboratories, conducting research in speech analysis, perception, and recognition. From 1977 to 1994, he was with Bell Northern Research, in a variety of management positions leading research and development activities in speech recognition, speech coding, and personal communications. From 1994 to 2000, he was the leader of the major program in personal and mobile communications of the Canadian Institute for Telecommunications Research.

He is a past associate editor for Speech Processing of the Journal of the Acoustical Society of America and Editor for Speech Communications of The IEEE TRANSACTIONS ON COMMUNICATIONS. He holds the Bell/Nortel/NSERC Industrial Research Chair in Personal Communications at INRS-Telecommunications, University of Quebec, Montreal, Canada.